The Cosmic Web and galaxy evolution around the most luminous X-ray cluster: RX J1347.5−1145

M. Verdugo,[1][*] M. Lerchster,[1,2] H. Böhringer,[1] H. Hildebrandt,[3,4,5] B. L. Ziegler,[6,7] T. Erben,[3] A. Finoguenov[1] and G. Chon[1]

[1]*Max Planck Institut für Extraterrestrische Physik, Giessenbachstrasse 1, 85748 Garching bei München, Germany*
[2]*University Observatory Munich, Ludwigs-Maximillians University Munich, Scheinerstrasse 1, 81679 Munich, Germany*
[3]*Argelander-Institut für Astronomie, University of Bonn, Auf dem Hügel 71, 53121 Bonn, Germany*
[4]*Sterrewacht Leiden, Leiden University, Niels Bohrweg 2, 2333 CA Leiden, the Netherlands*
[5]*University of British Columbia, Department of Physics and Astronomy, 6224 Agricultural Road, Vancouver, BC V6T 1Z1, Canada*
[6]*European Southern Observatory, Karl-Schwarzschild-Strasse 2, 85748 Garching bei München, Germany*
[7]*University of Vienna, Department of Astronomy, Türkenschanzstrae 17, 1180 Vienna, Austria*

ABSTRACT

In this paper we study large-scale structures and their galaxy content around the most X-ray luminous cluster known, RX J1347.5−1145 at $z = 0.45$. We make use of $u*g'r'i'z'$ Canada–France–Hawaii Telescope (CFHT) MegaCam photometry together with VIsible MultiObject Spectrograph (VIMOS) Very Large Telescope (VLT) spectroscopy to identify structures around RX J1347 on a scale of $\sim 20 \times 20$ Mpc^2. We construct maps of the galaxy distribution and the fraction of blue galaxies. We study the photometric galaxy properties as a function of the environment traced by the galaxy density. We identify group candidates based on galaxy overdensities and study their galaxy content. We also use available *Galaxy Evolution Explorer* (*GALEX*) near-ultraviolet imaging to identify strong unobscured star-forming galaxies. We find that the large-scale structure around RX J1347 extends in the north-east–south-west direction for at least 20 Mpc, over a region in which most of the group candidates are located, some of which show X-ray emission in archival *XMM–Newton* observations. As in other studies, we find that the fraction of blue galaxies (F_{blue}) is a function of galaxy number density, but the bulk of the trend is due to galaxies belonging to massive systems. The fraction of ultraviolet- (UV-) bright galaxies is also a function of environment, but their relative number compared with the blue population seems to be constant regardless of the environment. These UV emitters also have similar properties at all galaxy densities, indicating that the transition between galaxy types occurs over short time-scales. Candidate galaxy groups show a large variation in their galaxy content and F_{blue} in those groups displays little dependence on galaxy number density. This may indicate possible differences in their evolutionary status, or suggest that the processes acting in groups are different from those in clusters. The large-scale structure around rich clusters provides a dynamic environment for galaxy evolution. In the case of RX J1347, the transformation may start within infalling groups and finish with the removal of the cold gas once galaxies are accreted into massive systems.

Key words: galaxies: clusters: general – galaxies: clusters: individual: RX J1347.5−1145 – galaxies: evolution.

1 INTRODUCTION

Galaxy properties, such as spectral type and morphology, are known to correlate with environment: the central regions of galaxy clusters are mainly composed of bulge-dominated, passive evolving, red galaxies, whereas the low-density field is preferentially inhabited by disc-like, blue, active star-forming types (e.g. Dressler 1980; Dressler, Thompson & Shectman 1985). This behaviour has been studied in the local and distant Universe out to large cluster-centric distances (Balogh et al. 1999; Christlein & Zabludoff 2005; Poggianti et al. 2008; Verdugo, Ziegler & Gerken 2008; von der Linden et al. 2010; Bauer et al. 2011). Some of these studies have shown that the decline in the star-formation activity starts too far

[*]E-mail: mverdugo@mpe.mpg.de

away from the cluster cores to be caused only by cluster-specific processes and some form of preprocessing would be necessary to account for the difference in galaxy populations.

Going to higher redshifts, it is observed that the fraction of blue galaxies in distant clusters increases with redshift (Butcher & Oemler 1978). At first order this result indicates an increase of the star-formation activity within clusters, which has recently been confirmed by studies looking at the mid-infrared signatures of star formation (Saintonge, Tran & Holden 2008; Haines et al. 2009a; Finn et al. 2010). As the overall star-formation density was higher in the distant Universe, an obvious explanation would link this effect to a higher rate of infall of active galaxies into clusters from their surroundings, as predicted by the hierarchical build-up of structures in modern cosmologies (Ellingson et al. 2001).

However, systematic studies of the cluster population have often been handicapped by the large cluster-to-cluster variation at all epochs, which displays little or no correlation with total mass (e.g. Popesso et al. 2007; Poggianti et al. 2008; see however Hansen et al. 2009). Detailed analysis of clusters with similar global properties shows that they can contain a rather different galaxy population (e.g. Moran et al. 2007; Braglia et al. 2009). It may be possible that the cluster galaxy content depends on more subtle aspects of cluster nature, such as assembly history, substructure and the surrounding large-scale structure.

Recently a number of studies have begun to investigate the galaxy populations embedded in the filamentary structure around clusters. By far the most complete sample was published by Porter et al. (2008), where a large catalogue of filaments drawn from the Two-degree-Field Galaxy Redshift Survey (2dFGRS) was studied. They found a sharp increase of star-formation activity in filaments joining clusters at approximately 2–3 Mpc from the nearest cluster centre. Similarly Mahajan, Haines & Raychaudhury (2010) report an increase of star-formation activity among dwarf blue galaxies in the infall regions of the Coma supercluster.

At moderate redshifts, Braglia, Pierini & Böhringer (2007) have found a number of bright, blue star-forming galaxies in filaments around two distant X-ray-luminous $z \sim 0.3$ clusters drawn from the REFLEX–DXL (ROSAT ESO Flux-Limited X-ray Cluster Survey – Distant X-ray Luminous) sample (Zhang et al. 2006). Using the *Spitzer* satellite, Fadda et al. (2008) discovered a number of starbursts in a 'cluster-feeding' filament around a $z \sim 0.2$ cluster. Similarly, Koyama et al. (2008) report an increase of the number density of 15-μm sources detected with the *AKARI* space mission in medium-density environments in a cluster at $z \sim 0.8$. Marcillac et al. (2007) detected several dusty starbursts in the infall regions of another rich $z \sim 0.8$ cluster. Haines et al. (2009b) also find a number of obscured star-forming galaxies in the Abell 1758 ($z = 0.28$) cluster complex, coinciding with filaments and infalling groups. They also find that one of the subclusters (A1758N) is more active than the central one, probably reflecting different dynamical histories.

On the other hand, a detailed analysis of the Abell 901/902 supercluster ($z \sim 0.15$) by Gallazzi et al. (2009) and Wolf et al. (2009) shows that there is indeed an increase of obscured star-formation activity at intermediate densities, however it appears to be rather mild, as most of the galaxies have star-formation rates lower than or similar to those of normal blue star-forming galaxies.

In a complementary analysis, Li, Yee & Ellingson (2009) observed that the fraction of blue galaxies increases faster with redshift in groups associated with Canadian Network for Observational Cosmology (CNOC1) clusters (Yee, Ellingson & Carlberg 1996) than in the clusters themselves. Finally, Tanaka et al. (2007, 2009) have shown evidence of newly formed red galaxies with residual star for-

Table 1. Sumary of the CFHT/MEGACAM observations.

Program/PI	Filter	Exp. Time [s]	M_{limit} [a] [mag]	seeing [arcsec]
2006BH34/Ebeling	u^*	4260	25.09	0.95
2005AC10/Hoekstra	g'	4200	26.44	0.82
2005AC10/Hoekstra	r'	6000	25.94	0.77
2005AC12/Balogh	i'	1600	25.74	1.03
2005AC12/Balogh	z'	3150	24.80	1.14

[a] S/N = 5 in an aperture of 1 arcsec. Magnitudes are in the *AB* system.

mation in the large-scale structure around clusters, indicating that these systems may be very effective in transforming galaxies over cosmic time.

In this study we follow similar ideas. We surveyed an area of $\sim 20 \times 20 \, \text{Mpc}^2$ around the centre of the very rich cluster RX J1347.5−1145 at $z = 0.45$ (RX J1347 hereafter). This cluster is the most X-ray luminous one (Schindler et al. 1997) found in the REFLEX cluster survey (Böhringer et al. 2004) and has been investigated by different techniques, including strong and weak lensing (Bradač et al. 2005, 2008; Halkola et al. 2008; Lu et al. 2010; Medezinski et al. 2010), X-ray (Ettori, Allen & Fabian 2001; Gitti, Piffaretti & Schindler 2007b; Ota et al. 2008), radio (Gitti et al. 2007a), the Sunyaev–Zeldovich effect (Komatsu et al. 2001; Kitayama et al. 2004; Mason et al. 2010) and optical spectroscopy (Cohen & Kneib 2002; Lu et al. 2010).

Most of these studies have arrived at the conclusion that RX J1347 is likely one of the most massive objects in the Universe. In the context of the hierarchical growth of structures predicted by ΛCDM cosmologies, such a massive cluster should sit at the centre of a complex network of filaments and subclumps, as our first results indicate, making it an ideal target for our investigation.

Throughout this paper, we will use a cosmology of $H_0 = 70 \, \text{km s}^{-1} \, \text{Mpc}^{-1}$, $\Omega_{\text{m}} = 0.3$ and $\Omega_{\Lambda} = 0.7$.

2 OBSERVATIONS

2.1 Optical data

Our study makes use of available data taken with the MegaPrime camera mounted at the 3.6-m Canada–France–Hawaii Telescope (CFHT) using the $u^*g'r'i'z'$ filter set. The field of view of the instrument covers 1 deg^2, roughly $20 \times 20 \, \text{Mpc}^2$ at $z = 0.45$. The total usable field in our case is somewhat smaller (0.82 deg^2) due to the imperfect overlap of the target fields taken with the different filters. Table 1 contains a summary of the observations with this instrument. Fig. 1 shows the total field of view of the observations.

The MEGACAM data were retrieved from the Elixir system[1] in a preprocessed form from the Canadian Astronomy Data Centre (CADC[2]) archive and further processed as described in Erben et al. (2009) and Hildebrandt et al. (2009). The final data products consist of astrometrically and photometrically calibrated co-added science and noise-map data with the characteristics summarized in Table 1. Photometric zero-points for our data were provided by Elixir. We checked the calibration against colour–colour diagrams for model stars from the Pickles (1998) library. No offsets between the observed and theoretical stellar locus were appreciable, which would

---

[1] http://www.cfht.hawaii.edu/Instruments/Elixir/home.html
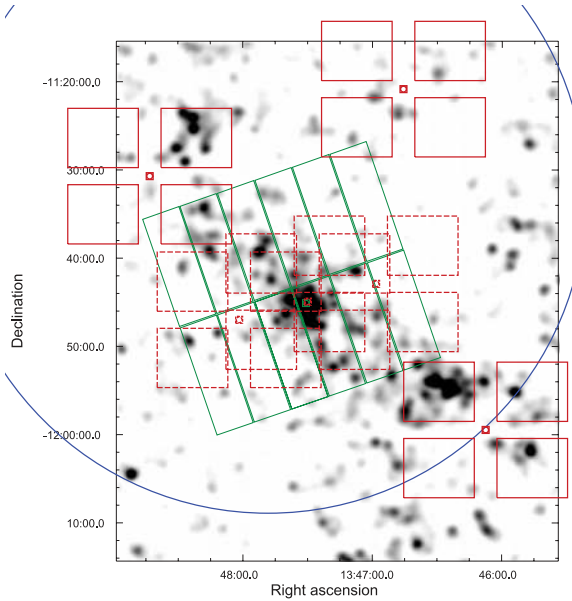[2] http://cadcwww.dao.nrc.ca/cadc/

Figure 1. Layout of the observations used in this paper, superimposed on the density map of cluster member candidates (Section 8). Dashed red rectangles represent VIMOS LR spectroscopy and solid ones are VIMOS MR masks. The large semi-circle shows the region covered by *GALEX*. The tilted green mosaic represent the *XMM–Newton* EPIC-pn observations.

indicate a bias in the calibration. Further corrections are described in Section 3.1.

A note about the filters. The u^* band at $z = 0.45$ covers a rest-frame wavelength range of 2400–2800 Å and would fall within the *Galaxy Evolution Explorer* (*GALEX*) near-ultraviolet (NUV) band at $z = 0$. The reddest band (the z filter) corresponds approximately to the r band in the rest frame. Finally, the 4000-Å break at $z = 0.45$ is well bracketed by the g and r bands.

Photometry was performed with SEXTRACTOR (Bertin & Arnouts 1996) in dual mode, using the deepest image (i.e. r' band) as a detection frame. Images have been convolved with a Gaussian filter to match the worst-seeing image. Galaxy colours have been extracted in a 2.5-arcsec aperture, which is equivalent to 14.4 kpc at $z = 0.45$. This is a good trade-off between an adequate sampling of the point spread function (PSF) wings and the aperture size, so the noise for fainter objects remains limited.

The photometric catalogue contains almost 60 000 sources, including 6890 stars according to the SEXTRACTOR CLASS_STAR parameter (CLASS_STAR ≥ 0.95), which is reliable down to $r \sim 23$. Those stellar sources were eliminated from the catalogue. Stars fainter than this limit were eliminated using an additional approach (see Section 3).

Galactic extinction for each filter was calculated using the dust maps of Schlegel, Finkbeiner & Davis (1998).

Comparisons of number counts with other photometric surveys of greater depth, like the Canada–France–Hawaii Telescope Legacy Survey Deep Synoptic Survey (CFHTLS–Deep: Ilbert et al. 2006; Coupon et al. 2009), indicate that our photometric catalogue is complete down to $r' = 23.5\,AB$. Fainter sources are thus removed from the catalogue.

2.2 Spectroscopy

Spectroscopy in the field was performed with the VIsible MultiObject Spectrograph (VIMOS) at the European Southern Observatory

(ESO) Very Large Telescope (VLT) using the low-resolution blue grism (LR-Blue, PID: 169.A-0595, PI: Böhringer) and the medium-resolution one (MR, PID: 381.A-0823, PI: Verdugo).

The first programme covered the central regions with an overlapping pattern to fill the gaps between the VIMOS CCDs properly (see Fig. 1). The individual target selection was based on the *I*-band magnitudes of the galaxies.

The second programme targeted the large-scale structures first identified using colour-selected galaxies with the MEGACAM photometry. The individual object selection was colour-based, excluding objects redder than the cluster red sequence. In practice, the galaxy distribution and mask design constraints do not allow the selection of all candidate objects with desirable photometric properties, leaving empty regions in which we placed additional slits, so that up to 40 per cent of the galaxies were selected randomly.

Data reduction was carried out using the VIPGI pipeline (Scodeggio et al. 2005) and redshifts have been obtained using the EZ software (Garilli et al. 2010) and custom-made tools. In total we secured 745 redshifts. The distribution of galaxies with spectroscopic redshift is presented in the upper panel of Fig. 2. Our spectroscopic campaign over the full 1 deg^2 field was recently completed and results will be presented in a forthcoming paper.

We have also added 62 out of the 79 redshifts previously published by Cohen & Kneib (2002) using Keck spectroscopy in the very central regions of the cluster, making a total of 807 redshifts. The remaining 17 redshifts are also common to our data set.
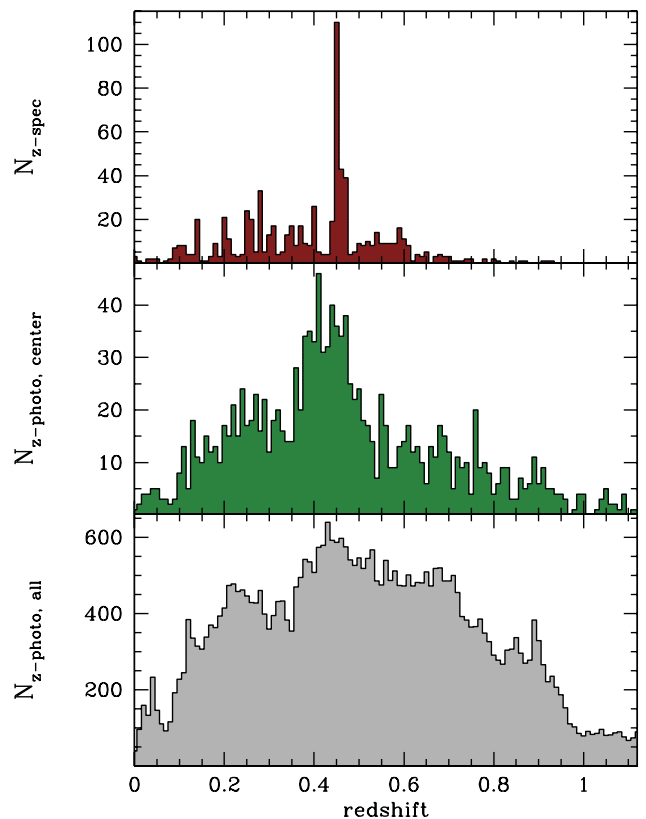

Figure 2. Upper panel: distribution of spectroscopic redshifts from our VIMOS observations. Middle panel: photometric redshift distribution for all galaxies in the central 10 arcmin. Lower panel: histogram of photometric redshifts for all galaxies with $r \leq 23.5$ mag.

2.3 *GALEX* observations

Observations with *GALEX* were found in the MultiMission Archive at the Space Telescope Science Institute (MAST) archive under programme GI3_103 (PI: Hicks, see also Hicks, Mushotzky & Donahue 2010 for more details). Both NUV ($\lambda_{eff} = 2267\,\text{Å}$) and far-ultraviolet (FUV: $\lambda_{eff} = 1516\,\text{Å}$) bands were exposed for 9120 s. At $z \sim 0.45$ the NUV filter is similar to the rest-frame FUV filter and thus a good indicator of the unobscured star-formation activity.

The limiting magnitude of the NUV observations (NUV = 24 *AB* at 3σ) is deep enough to detect the strongest star-forming galaxies at $z \sim 0.45$, however the coverage of our field is imperfect (see Fig. 1). FUV observations are much shallower and will not be used in this work.

From the catalogues produced by the *GALEX* pipeline (Morrissey et al. 2007) we extracted all sources with at least 3σ detection significance. Objects with distances larger than $0.58°$ from the field centre were eliminated to avoid artefacts present at the field edges.

We matched the NUV sources with our optical photometric catalogue using a search radius of 3.5 arcsec. Increasing the search radius, due to the broader *GALEX* PSF, does not produce more matches and contamination appears beyond 5 arcsec. Matched objects were also visually inspected against the *u*-band image to check the purity of the catalogue. In total, we matched 1040 objects with $0.37 < z_{phot} < 0.52$, our cluster galaxy selection window (see Section 3).

2.4 X-ray data

RX J1347 has been observed with the *XMM–Newton* X-ray telescope (ObsID:0112960101, PI: M. Turner) for 38 ks total time. Results of these observations have been reported elsewhere by Gitti & Schindler (2004) and Gitti et al. (2007b).

The *XMM–Newton* observations were focused on the central cluster and thus only a fraction of the field is covered by them (see Fig. 1). Nevertheless, they represent an opportunity to detect the X-ray emission associated with the large-scale structures around RX J1347.

We have processed the imaging using custom-made software. After flare cleaning, following Zhang et al. (2004), we retained 24, 31 and 30 ks of clean time for EPIC-pn, MOS1 and MOS2, respectively. The background has been estimated using the regions of the observation free of cluster emission and point sources. We have iterated on the definition of the background zone, as in Bielby et al. 2010, by also removing the zone of excess X-ray emission associated with the location of the large-scale structure (see Section 5.3 and Fig. 8 later).

In this paper we use the wavelet+PSF restoration-image technique of Finoguenov et al. (2010). The objective is to report the properties of the optically selected groups (see Section 5.2) using the residual flux image after background and point-source removal (including the PSF wings).

3 CLUSTER MEMBER SELECTION

3.1 Photometric redshifts

The only way to establish cluster membership with high confidence is by using information from spectroscopic observations. Unfortunately, obtaining a complete sample of galaxies is very time-consuming and difficult to perform down to faint magnitudes. For that reason, in this work we use the photometric information from our multicolour imaging.

We use the code LePhare (Ilbert et al. 2006) to obtain photometric redshifts (z_{phot}) for all sources down to $r \sim 23.5$ mag using only the optical data. Because of the similar characteristics of our data, we have followed the procedures of Ilbert et al. (2006) to obtain photometric redshifts. In particular, we have used the same improved galaxy templates that they used for estimating redshifts for the CFMT Legacy Survey (CFHTLS). Since the *GALEX* data do not cover the whole field, they have not been used to obtain photometric redshifts.

We have also used spectroscopic redshifts to optimize the templates and to compensate for the systematic errors in the photometry. The results from LePhare have been compared with photometric redshifts obtained using BPZ (Benítez 2000, see also Hildebrandt et al. 2009) and PHOTO-Z (Bender et al. 2001, see also Lerchster et al. 2011). The results of the three codes agree within the statistical uncertainties.

In Fig. 2 we plot the distribution of photometric redshifts for the whole field and the central 10 arcmin. A clear peak in the redshift distribution centred at $z \sim 0.45$ can be discerned. As a comparison we plot the distribution of the spectroscopic redshifts in the upper panel.

LePhare also provides information on the object type, via classification of their spectral energy distribution (SED). This helped us to eliminate stars from the photometric catalogue below the limit of the CLASS_STAR SExtractor parameter, as stellar templates have also been included in the analysis. As galaxies dominate the number counts at faint magnitudes, we expect that star contamination is very low in our sample.

To assess the quality of the photometric redshifts, we plot in Fig. 3 a comparison between z_{spec} and z_{phot} as a function of z_{spec}. The regions marked by lines show $|z_{phot} - z_{spec}| < 0.05(1 + z_{spec})$ and $|z_{spec} - z_{phot}| < 0.15(1 + z_{spec})$ respectively. Photometric redshifts with $|z_{spec} - z_{phot}| > 0.15(1 + z_{spec})$ are considered catastrophic outliers.

A number of statistical tests have been proposed in the literature (e.g. Ilbert et al. 2006; Pelló et al. 2009) to probe the quality of the photometric redshifts.

(i) The fraction of catastrophic outliers is defined as $|z_{spec} - z_{phot}| > 0.15(1 + z_{spec})$. The result is 9.12 per cent.

(ii) The normalized median absolute deviation $\sigma_{z,\text{NMAD}} = 1.48 \times$ median $[|z_{spec} - z_{phot}|/(1 + z)]$. The result is 0.037.

(iii) The systematic deviation between z_{phot} and z_{spec} $\langle \Delta(z) \rangle = \sum (z_{spec} - z_{phot})/N$, with $\Delta_z = |z_{spec} - z_{phot}|$. Catastrophic outliers are excluded. The result is 0.0051.

(iv) The standard deviation of $\Delta(z)$: $\sigma_z = \sqrt{(\Delta(z) - \langle \Delta(z) \rangle)^2/(N - 1)}$. The result is $\sigma_z = 0.058$. This value represents the scatter between spectroscopic and photometric redshifts.

These statistical tests show that the precision of our results is comparable to that obtained with similar data (see e.g. Ilbert et al. 2006) and the photometric redshifts display no bias compared with the spectroscopic ones. Still, they contain large uncertainties compared with the spectroscopic redshifts and therefore any selection will introduce contamination by field interlopers and loss of cluster members.
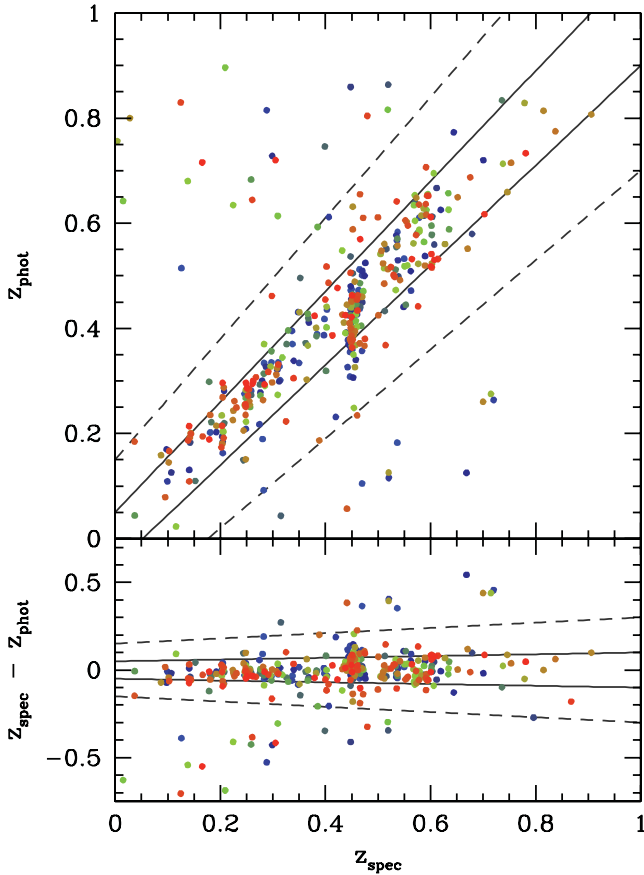
Figure 3. Comparison between photometric redshifts and the 807 spectroscopic redshifts. The solid lines mark where $|z_{spec} − z_{phot}| < 0.05(1 + z)$ and the dashed ones $|z_{spec} − z_{phot}| < 0.15(1 + z)$. Outside this latter limit, photometric redshifts are considered catastrophic. The colours of the points indicate the best-fitting templates, with redder colours for earlier galaxy types. The mean scatter of z_{phot} is $\sigma_z = 0.058$.

3.2 Optimal redshift window and statistical background subtraction

As a first step, we select galaxies with photometric redshifts within an optimal range. This is done by dividing the spectroscopic sample into cluster members ($0.43 < z_{spec} < 0.48$)[3] and non-members. Then we compare the fraction of retained members and rejected non-members as a function of *increasing* z_{phot} window threshold ($\Delta z = |z_{cl} − z_{thres}|$). The contamination due to non-members is also calculated. The results of this procedure are presented in Fig. 4, where we plot the *photometric redshift* distribution for spectroscopic cluster members and non-members. In the inset, we plot the fraction of retained members, rejected non-members and contamination as a function of z_{phot} window size.

This procedure is inspired by the selection scheme of Pelló et al. (2009). In contrast to us, they used the full z_{phot} probability function. In our case the probability functions calculated by LePhare are, in general, too narrow and likely not reliable, despite the fact that their peak values are statistically accurate, as shown in Fig. 3.

The optimal threshold is $\Delta z = 0.07$, where ∼80 per cent of the spectroscopic members are retained and a similar fraction of
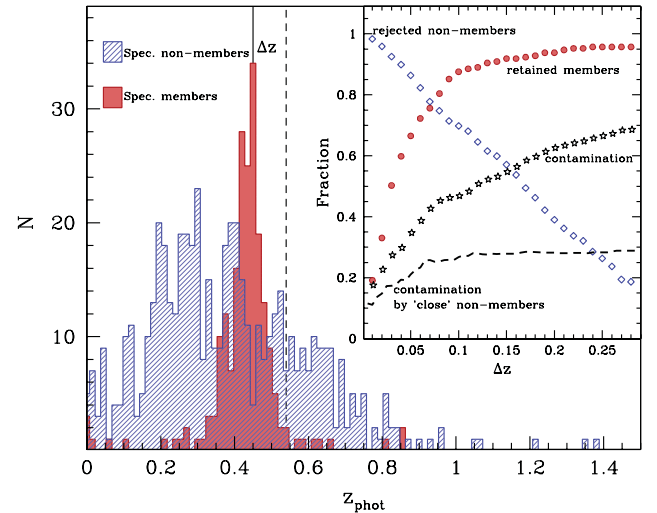
---

[3] This larger range is necessary because of a possible associated structure at $z = 0.47$, see Section 5.

Figure 4. Photometric redshift distribution for spectroscopic confirmed members (red filled histogram) and non-members (blue hashed one). The inset shows the fraction of retained members (red circles) and rejected non-members (blue diamonds) as a function of an increasing z_{phot} window threshold. The contamination due to all galaxies (black stars) is also displayed. The contamination by 'close non-members' (dashed line) refers to non-cluster galaxies with $0.38 < z_{spec} < 0.52$, i.e. the same redshift range we finally chose to select our cluster galaxies.

non-members are rejected. The contamination by non-members is ∼45 per cent, however more than half of this contamination (roughly 55 per cent) comes from 'close' non-members, i.e. field galaxies with spectroscopic redshifts within the threshold ($z_{spec} = 0.45 \pm 0.07$), which are difficult to distinguish through photo-z techniques.

This final catalogue of candidate cluster members contains 5895 sources down to $r = 23.5\,AB$.

To correct for contamination by field interlopers, we perform a statistical background subtraction following Pimbblet et al. (2002). For this, we use two areas of the field where the galaxy density is the lowest (see Fig. 8 later) to represent the field population. The total area used for this purpose is $0.285\,deg^2$.

We construct two colour–magnitude diagrams with the galaxy distribution binned in intervals of 0.1 mag in $(g − r)$ colour and 0.25 in r magnitude. One diagram corresponds to the whole cluster area and another only to the field. Both are normalized by their respective total areas.

Afterwards, the normalized field colour–magnitude diagram is divided by the cluster one (which also contains a field signal). The result can be interpreted as the probability that a galaxy belongs to the field as a function of colour and magnitude. In other words,

$$P(\text{Field})_{col,mag} = \frac{N(\text{Field})_{col,mag}}{N(\text{Cluster} + \text{Field})_{col,mag}}. \tag{1}$$

Note that this procedure is also valid in the presence of incompleteness as the field and cluster signal should have a similar level of incompleteness. Based on the probability map, we construct 100 Monte Carlo realizations of the parent catalogue. This is done by generating a random number between 0.0 and 1.0 for each galaxy and comparing it with its field probability according to its colour and magnitude. If this number is larger than $P(\text{Field})_{col,mag}$, the galaxy is attributed to the field population and thus eliminated from the cluster catalogue. Each resulting catalogue contains between 4000 and 4400 galaxies, which should represent the true cluster population. The different quantities presented in this paper are calculated

separately for each individual catalogue and then averaged. Error bars are then the standard deviation of these quantities.

3.3 The effect of the (in)accuracy of photometric redshifts

This study is based on a complete catalogue of cluster galaxies selected using moderately accurate and unbiased photometric redshifts. We have been careful in the selection of an optimal redshift bin that maximizes completeness and minimizes contamination. Still, the large redshift bin of $0.38 < z_{phot} < 0.52$ is equivalent to a transverse distance of ~ 450 Mpc (comoving), much larger than the extent of the large-scale structure around RX J1347. Superposition of unassociated systems is therefore expected and this should be kept in mind when interpreting the results.

The use of statistical background subtraction, by using 100 Monte Carlo generated catalogues, should correct for the *mean* contamination of the unassociated field. As different quantities are calculated for the individual 100 catalogues and averaged afterwards, the associated error bars should also include the uncertainty due to field contamination for a particular position of the field.

Larger than expected background fluctuations are of course difficult to assess and correct. We expect that superposition affects low-density areas more strongly than high-density ones like cluster cores.

4 GALAXY COLOURS AND LUMINOSITY FUNCTION

Old, passive, early-type galaxies are typically located in a narrow region within the appropriate colour–magnitude diagram, usually well described by a straight line leading to the so-called red sequence (Baum 1959; Gladders et al. 1998).

To isolate galaxies belonging to the red sequence, we ran LePhare on the spectroscopic catalogue, this time keeping the redshift fixed. This reduces the degrees of freedom for the χ^2 template fitting, yielding, in principle, more accurate estimates of the galaxy spectroscopic types. From the resulting catalogue we selected galaxies at $z_{spec} = 0.45 \pm 0.03$ with templates compatible with early types. We fitted a line to the colour–magnitude relation using a simple least-squares algorithm with 3σ clipping in five iterations. Under these conditions this method is accurate enough for our purposes. The results can be seen in Fig. 5. The red sequence is well approximated by the following relation: $(g - r) = -0.016 \times r + 1.77$ with a scatter of $\sigma = 0.067$ mag.

Based on the previous fit, we define red galaxies as all galaxies with colours redder than the lower 3σ limit (i.e. 0.201 mag) and blue otherwise. This limit will be used to calculate the fraction of blue galaxies in the following sections. Note that this definition is identical to the original scheme proposed by Butcher & Oemler (1978).

The colour–magnitude diagram for all spectroscopic members is plotted in Fig. 5. We also plot the distribution of all photo-z selected members. The bimodality of galaxy colours reported by several authors (e.g. Baldry et al. 2006; Loh et al. 2008) is also clearly discernible here.

In Fig. 6 we plot the distribution of *GALEX* NUV sources in the optical colour–magnitude diagram. Practically all detected sources correspond to blue galaxies. More luminous NUV sources tend also to be brighter and bluer in the optical. As a comparison, we also plot the distribution of all candidate cluster galaxies. It is evident that *GALEX* sources represent only a small subset of the galaxy population, probably the strongest, unobscured starbursts.
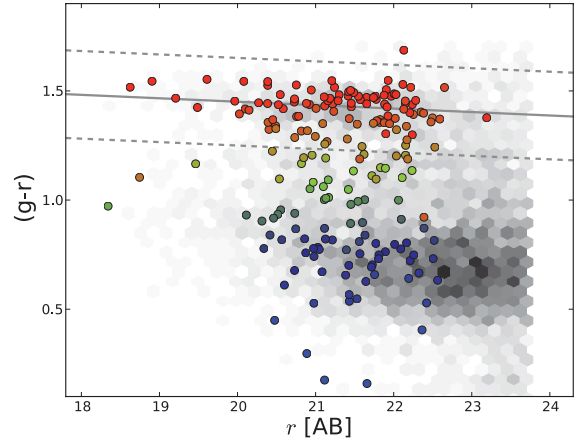

Figure 5. Observed colour–magnitude relation for spectroscopic members of RX J1347. Each galaxy has been colour-coded according to its best-fitting template, with redder colours for earlier types. The solid line marks the line that best describes the red-sequence fit to early-type galaxies. The dashed lines are the upper and lower 3σ limits. The colour distribution of all photo-z selected members is shown in grey-scale in the background.
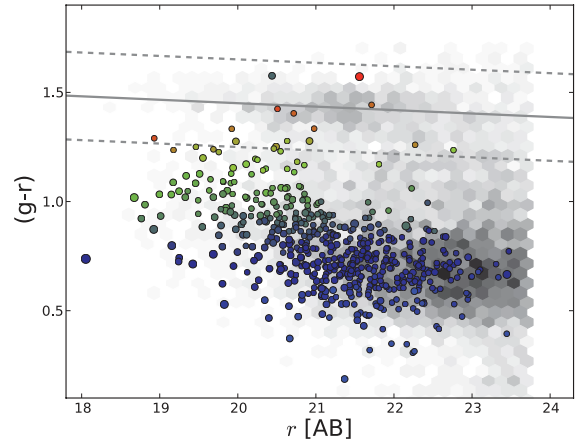

Figure 6. Colour–magnitude diagram for NUV *GALEX* detections with z_{phot} similar to the cluster. They have been colour-coded according to the best-fitting template. The sizes of the symbols are a function of the NUV magnitude. As a comparison, we plot in the background the colour–magnitude diagram for all candidate cluster galaxies from the photo-z selection.

We also calculate the rest-frame *i*-band luminosity for all, red and blue galaxies within $2R_{200}$ (4.6 Mpc) of the centre of RX J1347. Absolute magnitudes were obtained using the observed magnitudes and colours and applying typical *k*-corrections obtained with the online tool of Chilingarian, Melchior & Zolotukhin (2010).[4] The frequency of galaxies per 0.5 mag bin was fitted with a Schechter function (Schechter 1976) of the form

$$\phi(M)\,dM = 0.4\ln 10 \times \phi^\star \times 10^{-0.4(M-M^\star)(\alpha+1)}$$
$$\times \exp[-10^{-0.4(M-M^\star)}]\,dm, \qquad (2)$$

where $\phi^\star$ is the normalization factor, $M^\star$ is the characteristic magnitude and α describes the faint-end slope. The fitting was performed with a χ^2 minimization algorithm. The luminosity functions and the best-fitting Schechter parametrizations can be seen in Fig. 7. The

---

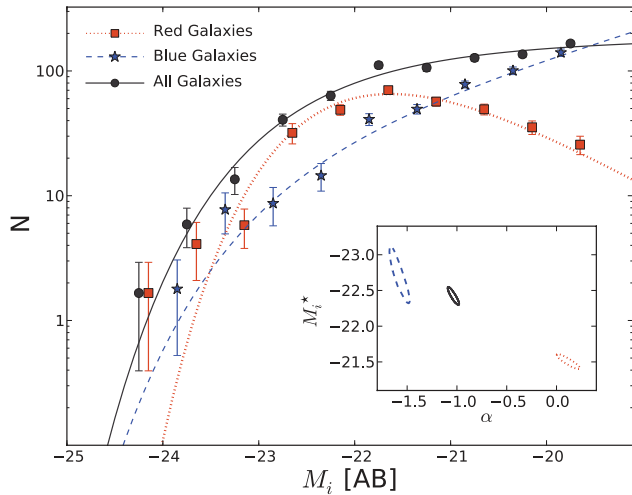[4] http://kcor.sai.msu.ru/UVtoNIR.html

Figure 7. Rest frame *i*-band luminosity function for all, red and blue galaxies within $2R_{200}$ (i.e. 4.6 Mpc) from the centre of RX J1347 with the best-fitting Schechter function overplotted. The inset shows the 1σ uncertainty contours for every fit.

results for the key parameters $M^{\star}$ and α are the following.

(i) All galaxies: $M^{\star} = -22.4 \pm 0.1$ mag, $\alpha = -1.04 \pm 0.06$.
(ii) Red galaxies: $M^{\star} = -21.5 \pm 0.1$ mag, $\alpha = 0.11 \pm 0.12$.
(iii) Blue galaxies: $M^{\star} = -22.7 \pm 0.4$ mag, $\alpha = -1.58 \pm 0.10$.

The values for $M^{\star}$ are in general agreement with the stacked luminosity function for $0.4 < z < 0.8$ clusters (see Rudnick et al. 2009 and references therein), although the luminosity function for red galaxies in RX J1347 displays a shallower faint-end slope than the (less massive) clusters studied by the previous authors.

5 THE CLUSTER ENVIRONMENT AND THE LARGE-SCALE STRUCTURES AROUND RX J1347

5.1 Galaxy number density and map of the galaxy distribution

We use the projected galaxy number density (Dressler 1980) as a measure of the environment. For each galaxy we calculate the area of the circle of radius r that encloses the 10th neighbour, so the density is defined as

$$\Sigma_{10} = \frac{11}{\pi r_{10}^2}. \tag{3}$$

This quantity was calculated for each of the 100 Monte Carlo realizations of the photo-z cluster catalogue (Section 3).

We preferred to use the 10th neighbour instead of the more usual fifth, as projection is an issue in a photo-z-selected catalogue. Using more galaxies reduces, in principle, the effects of shot noise, limiting these uncertainties.

This method can also be generalized to calculate the density for each point of a grid to produce a map of the galaxy density distribution (see Fig. 8). This procedure was called 'cluster tomography' by Pelló et al. (2009) and can be considered analogous to the method used by Haines et al. (2006b) to investigate the environment in the Shapley supercluster. It allows us to sample the high-density regions with adequate resolution without increasing the noise in the low-density ones. It can, therefore, be regarded as an adaptive smoothing method, with the advantage that it conserves the number density of galaxies at each position of the grid.

The first contour was defined at the mean density plus 1σ of the CFHTLS–Deep fields (Coupon et al. 2009). Taking mean and standard deviation of the four fields, we obtain a value of $\sim 11 \pm 4$ galaxies Mpc^{-2} at $z = 0.45$, using the same magnitude ($r < 23.5$) and photometric redshift cuts ($0.38 < z_{\mathrm{phot}} < 0.52$). Note, however, that the underdense areas in our field (marked with dashed rectangles in Fig. 8), have an average density of $\sim 9 \pm 3$ galaxies Mpc^{-2}, determined from statistics of the 100 Monte Carlo realizations from the parent catalogue. This makes the first contour 2σ over the background.

This map helps us to visualize the complex dynamical situation around RX J1347. The overdensity extends approximately in a diagonal across the field ~ 20 Mpc. Some filaments and several overdense subclumps can be seen, mainly along this large-scale structure. Some of the overdensities coincide with previously identified cluster candidates.

Besides the main cluster, two other galaxy concentrations are prominent: one towards the south-east, coincident with the cluster LCDCS 0825 (Gonzalez et al. 2001) and another towards the northeast without previous identification, which we will call in this paper 'the NE Clump'.

5.2 Groups of galaxies

Candidate galaxy groups were detected using the Voronoi–Delaunay tessellation technique (VTT) of Ramella et al. (2001) applied to the cluster photometric catalogue. The main advantage of this method is that it does not assume any particular physical properties of groups as do other techniques. This allows us to select galaxy concentrations with different galaxy content and morphologies. It is also very efficient in detecting galaxy overdensities in inhomogeneous backgrounds, according to the simulations of Sloan Digital Sky Survey (SDSS) fields by Kim et al. (2002). They also find that the efficiency of the VTT is greatly enhanced if galaxies are pre-selected in colour space, because of the improved background contrast and smaller contamination. Variations of this technique have been successfully used to produce galaxy cluster candidate catalogues either in redshift space (e.g. Marinoni et al. 2002) or through photometric selection (e.g. Geach, Murphy & Bower 2011b).

The VTT of Ramella et al. (2001) is based on splitting the two-dimensional (2-D) distribution of galaxies into independent cells, each containing only one galaxy. Galaxy group candidates are selected from adjacent cells that satisfy a certain density threshold over the cumulative Kiang distribution (Kiang 1966) of randomly positioned points. Once a significant number of cells have been associated, the overdensity is expanded circularly to include more galaxies until the density falls under the threshold. The radius of these circles (R_{group}) will be interpreted as the group physical size.

We select overdensities that are significant at the 90 per cent confidence level (c.l.), i.e. they form part of the top 90 per cent of the density distribution. This level is higher than the one originally proposed by Ramella et al. (2001), which was the 80 per cent c.l. We reject overdensities with probabilities larger than 20 per cent of being a random fluctuation, as we have already eliminated most of the contamination. We note, however, that our results are resistant to variation in these choices.

The group detection was performed in the parent catalogue but individual quantities are calculated for each of the 100 Monte Carlo realizations of the cluster catalogue. We do not claim that all of these groups are necessarily physical associations, as this would require spectroscopic confirmation. They also may be unassociated with
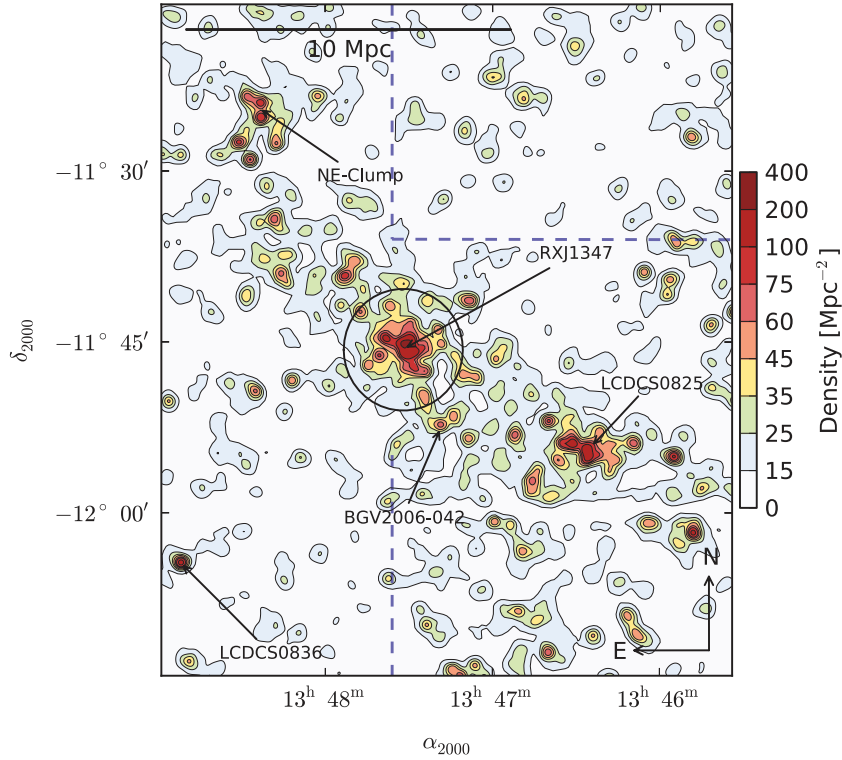
Figure 8. Map of the galaxy number density in Mpc^{-2} produced by the nearest-neighbour counting technique. This map is the combination of 100 individual background-subtracted maps. The first contour starts at the mean of the general field at $z \sim 0.45$ plus 1σ, obtained from CFHTLS (Coupon et al. 2009), and 2σ over the low-density regions marked with dashed rectangles. These regions were used for statistical background subtraction (see Section 3). Note that the overdensity associated with the central cluster runs in diagonal across the field, where a complex network of filaments and subclumps can be seen. Previously detected cluster candidates associated with overdensities at $z \sim 0.45$ have been marked, including the central cluster. The circle around RX J1347 marks $R_{200} = 2.3$ Mpc from Gitti et al. (2007b).

the cluster, however they allow us to probe particular environments. In total, we detect 34 group candidates.

Due to the lack of reliable mass measurements and possibly differences in their galaxy content, group candidates will be characterized by two parameters:

(i) the mean density of galaxies, calculated by counting the number of galaxies within R_{group} (note that this number differs from the Σ_{10} indicator introduced in the previous section) and

(ii) the total rest-frame i-band luminosity, obtained by summing the individual galaxy luminosities within R_{group}, as a proxy of the total stellar content.

The errors in both quantities are estimated from the statistics of the 100 Monte Carlo catalogues. Comparison of different density estimates is provided in Appendix A.

In Fig. 9, we plot the distribution of the candidate groups over the density map of the field. Most of the groups are located along the large-scale structure, but some are also quite isolated. The different colours indicate their different galaxy content, with red solid circles marking groups dominated by early-type galaxies, green ones an intermediate galaxy mix and blue ones groups dominated by blue galaxies (see Section 8.3 for more details). Properties of the group are summarized in Table B1.

5.3 The large-scale structure

The overdensity associated with the cluster extends diagonally across the field for about 20 Mpc. As we also want to study the

effects of the filamentary structure on galaxy evolution, we isolate galaxies belonging to this structure. This is done by modelling it with two polynomial functions that encompass most of the groups found in the large-scale structure (see Fig. 9). Distance is measured from the south-west corner towards the north-east, with RX J1347 roughly at the middle.

6 SEARCH FOR X-RAY EMISSION FOR OPTICALLY IDENTIFIED SYSTEMS

6.1 *ROSAT* All-Sky Survey

We performed an analysis of *ROSAT* All-Sky Survey (RASS) data around RX J1347 to see whether the two richer structures besides the central cluster (i.e. LCDCS 0825 and the NE Clump) have detectable X-ray emission. We measured the flux within the aperture given by the cluster-detection algorithm and keeping the position fixed, i.e. a forced detection. To measure the flux, we use two methods: (1) a wavelet technique as in Finoguenov et al. (2010), (2) the growth-curve analysis of Böhringer et al. (2000).

For LCDCS 0825, we find a 2σ detection with an upper limit for $F_{\mathrm{X},0.1-2.4\,\mathrm{keV}} < 1.15 \times 10^{-13}$ erg s^{-1} cm^{-2}, which implies a luminosity $L_{\mathrm{X},0.1-2.4\,\mathrm{keV}} < 1.2 \times 10^{44}$ erg s^{-1}. We take the L_{X}–M relation of Leauthaud et al. (2010):

$$\frac{\langle M_{200}E(z)\rangle}{M_0} = A\left(\frac{\langle L_{\mathrm{X}}E(z)^{-1}\rangle}{L_{\mathrm{X},0}}\right)^{\alpha}, \tag{4}$$

where $M_0 = 10^{13.7} h_{70}^{-1}$ M$_{\odot}$, $L_{\mathrm{X},0} = 10^{42.7} h_{70}^{-1}$ erg s^{-1}, $\log_{10}(A) = 0.068 \pm 0.063$ and $\alpha = 0.66 \pm 0.14$. This sets an upper limit of
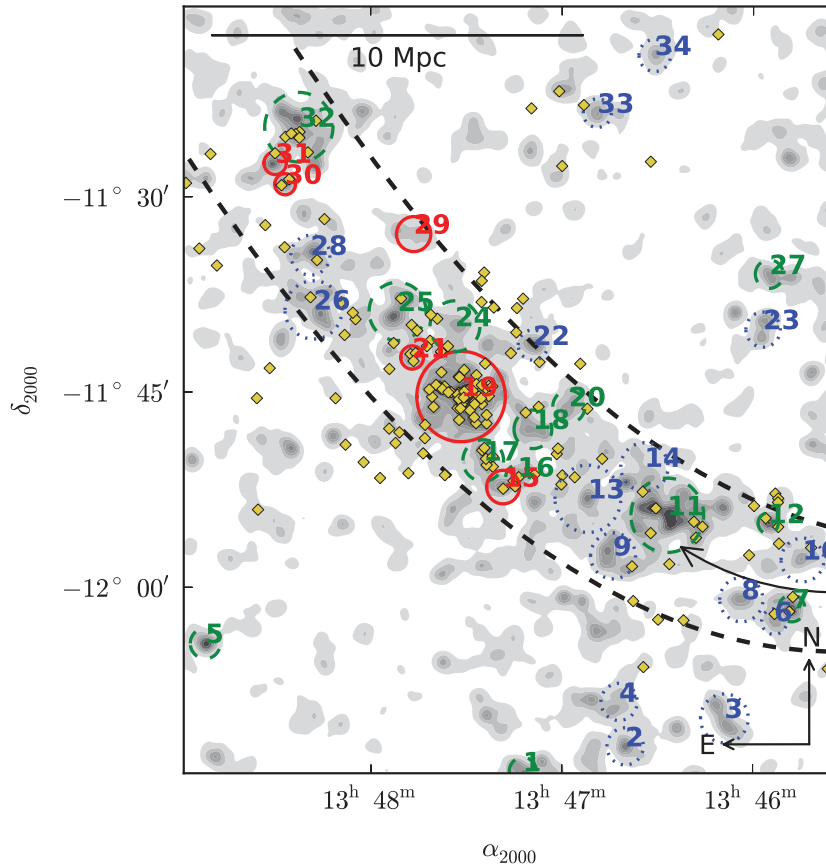
Figure 9. Distribution of the group candidates detected by the Voronoi–Delaunay algorithm over the density field. Contours are the same as in Fig. 8. The numbers are group IDs as listed in Table B1. Groups have been colour-coded according to their galaxy content: blue dotted circles represent groups with $F_{blue} > 0.75$, green dashed circles are groups with $0.75 > F_{blue} > 0.5$ and red solid circles are groups with $F_{blue} < 0.5$. The large area delimited by dashed lines marks large-scale structure associated with the cluster. The curved arrow indicates that distances along the LSS are measured from the lower right corner (south-west) towards the upper right one (north-east). Dots are galaxies with *spectroscopic* redshifts similar to the cluster. A zoom-in of the central regions is shown in Fig. 12.

$M < 3.1 \times 10^{14}\,M_\odot$, consistent (within the errors) with the reported weak lensing mass of Lu et al. (2010) (see more in Section 7.2). However, the low significance prevents us from setting further constraints.

The NE Clump (ID = 32) has a 1σ detection in the RASS imaging. The upper limit for its X-ray flux is $F_{X,0.1-2.4\,keV} < 8.5 \times 10^{14}\,erg\,s^{-1}\,cm^{-2}$ and the luminosity $L_{X,0.1-2.4\,keV} < 8.2 \times 10^{43}\,erg\,s^{-1}$. Using the same scaling relation, the upper mass limit is $M < 1.4 \times 10^{14}\,M_\odot$.

6.2 *XMM–Newton*

XMM–Newton observations cover the central regions of the field (see Fig. 1), tracing part of the large-scale structure associated with RX J1347. A number of optically selected group candidates are located in the region and we try to recover any X-ray emission from their warm–hot intergalactic medium.

As in the previous case, we performed a forced detection using information from the optical group detection algorithm. Point sources were removed and the background estimation (in the 0.5–2 keV range) was done using areas outside the cluster large-scale structure.

In total we were able to measure the flux with over 1σ significance for nine groups. The properties are summarized in Table B2. The flux errors are propagated to the luminosities and mass estimates.

The 20 per cent systematic uncertainty for the mass estimates (due to the relevant scaling relation) is not listed in the errors.

The X-ray significance map is shown in Fig. 12, with contours starting at 1σ per resolution element (32 arcsec × 32 arcsec). The X-ray emission for some of the groups might be the residual of the central cluster emission (groups 17, 18 and 22).

7 CLUSTERS BELONGING TO LARGE-SCALE STRUCTURES AROUND RX J1347

Some structures in the studied field have been previously recognized. Some of them match with detected overdensities at $z \sim 0.45$ and thus are possibly associated with RX J1347. We have marked their position in Fig. 8. In the following we provide an individual description for some of them.

7.1 RX J1347.5−1145

This cluster was serendipitously discovered by Schindler et al. (1995) as part of the REFLEX Cluster Survey (Böhringer et al. 2001) using the RASS. It also appeared as the first strong lensing system in the REFLEX identification optical imaging.

RX J1347 is also known as LCDCS 0829 in the Las Campanas Distant Cluster Survey (Gonzalez et al. 2001). Subsequent X-ray analysis with *XMM–Newton* has confirmed that it is indeed a
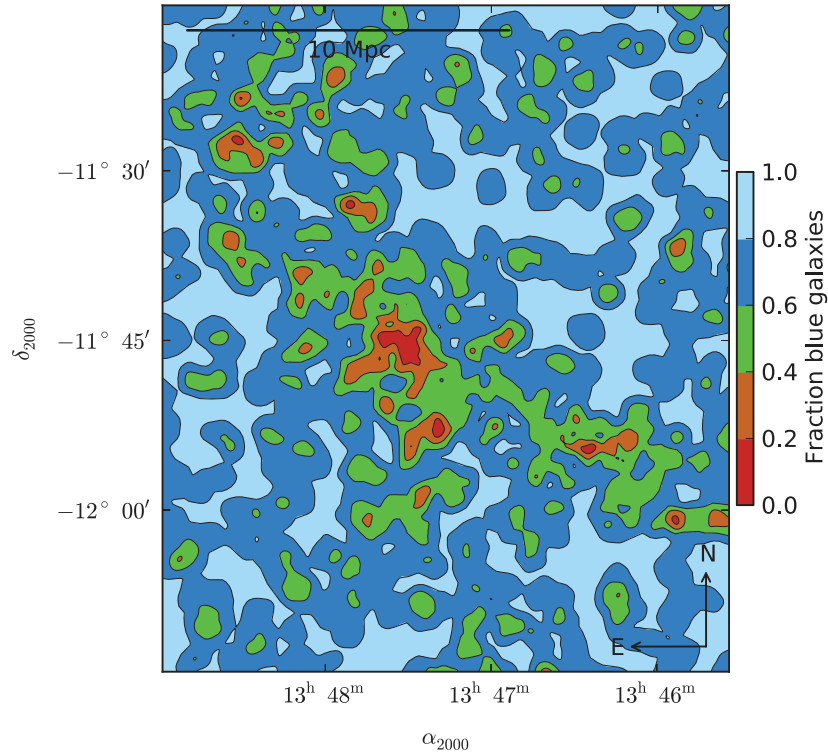
Figure 10. Map of the fraction of blue galaxies across the field. Compared with Fig. 8, the close relation between galaxy mix and environment can be noted: denser regions host larger fractions of red galaxies. This plot illustrates, however, the complexity of this relation.

massive structure with an X-ray luminosity in excess of $L_X = 6.0 \times 10^{45}$ erg s^{-1} in the 2–10 keV range, a temperature of $kT \sim 10$ keV and a mass estimate of $2.0 \pm 0.4 \times 10^{15}$ M$_\odot$ within the central 1.7 Mpc (Gitti & Schindler 2004). The same authors also find a massive cooling flow with a nominal accretion rate of ~ 1900 M$_\odot$ yr^{-1}.

Initial discrepancies in the mass derived using X-ray, strong and weak lensing analyses were solved by more recent studies using a combination of techniques as in Bradač et al. (2005, 2008). Furthermore, the initial low dynamical mass estimate ($\sim 4 \times 10^{14}$ M$_\odot$) of Cohen & Kneib (2002) appears to be solved in Lu et al. (2010) by using a larger spectroscopic sample, yielding a mass well over 10^{15} M$_\odot$ in concordance with the X-ray results.

In Fig. 13 we show the redshift distribution of the cluster members from our spectroscopy. A more detailed analysis of the cluster dynamics (including mass estimates) will be presented in a forthcoming paper using the newer spectra.

For the moment, we would like to add the optical mass estimate using the richness measurements following Reyes et al. (2008). The centre is taken as the peak of the X-ray emission from Schindler et al. (1997). As a first step we determine the richness N_{200}, which is the number of red-sequence galaxies within 1 Mpc h^{-1} brighter than $0.4L^\star$ (i.e. $M_i = -20.51$, see Fig. 7). From the statistical background-subtracted catalogues, we count $N_{200} = 86.9 \pm 3.1$ galaxies.

Then we calculate the radius $R_{200}^{\mathrm{gal}} = 0.156 \times N_{200}^{0.6} \, h_{70}^{-1}$ Mpc, where the galaxy density is 200 times the mean of the Universe[5] yielding a result of $R_{200}^{\mathrm{gal}} = 2.27$ Mpc. We iterate the richness estimator with this new radius, obtaining a richness measure of

$N_{200} = 154 \pm 5$ galaxies, which we finally use to estimate the mass from the formula

$$M_{200}^{N_{200}} = (2.03 \pm 0.11) \left(\frac{N_{200}}{20} \right)^{1.16 \pm 0.09} \times 10^{14} \, \mathrm{M}_\odot, \quad (5)$$

obtaining $M_{200}^{N_{200}} = 2.17^{+0.8}_{-0.6} \times 10^{15}$ M$_\odot$ (random and systematics errors included), which is consistent with the estimates using other means.

We calculate the mass-to-light ratio by summing the rest-frame i-band luminosities of all galaxies within 1.7 Mpc. The result is $L = 6.25 \pm 0.2 \times 10^{12}$ L$_\odot$. Comparing this with the reported X-ray-determined mass of Gitti & Schindler (2004), we obtain a mass-to-light ratio of $M/L = 320 \pm 64$ M$_\odot$ L$_\odot^{-1}$, which is typical for rich clusters (Girardi et al. 2002).

7.2 LCDCS 0825

This structure was previously identified as a tentative cluster by Gonzalez et al. 2001 as part of the Las Campanas Distant Cluster Survey. Lu et al. (2010) obtained a redshift $z \sim 0.47$ (RX J1347–SW in their analysis), which we confirm. This implies a comoving distance of ~ 62 Mpc to RX J1347.

Although the concentration of galaxies is evident between RX J1347 and LCDCS 0825, Lu et al. (2010) were unable to confirm whether both structures are physically connected or are drifting away with cosmic expansion. Lu et al. (2010) reported a velocity dispersion of $\sigma = 780 \pm 100$ km s^{-1} and a mass of $M_{200} = 3.4^{+1.4}_{-1.1} \times 10^{14}$ M$_\odot$ for LCDCS 0825, which would make it a relatively massive cluster. This mass is somewhat higher than that derived using the X-ray luminosity from the RASS data. However, we note that our X-ray detection has low significance and thus a large associated error (see Section 2.4). Alternatively, the

---

[5] This must not be confused with the r_{200} parameter, which refers to the matter density.
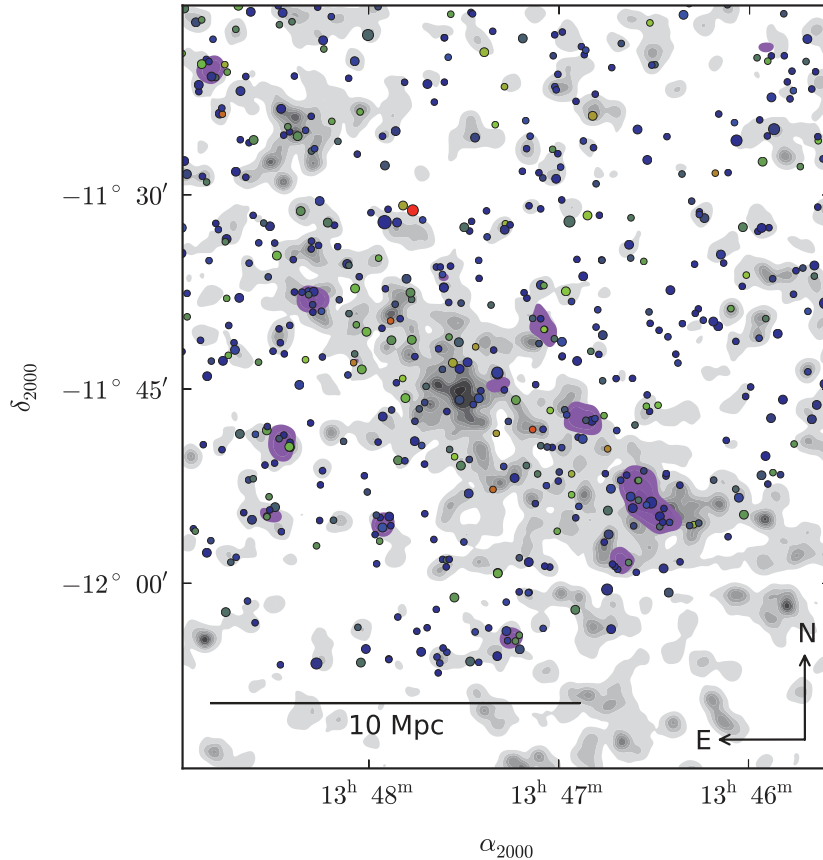
Figure 11. Distribution of *GALEX* NUV sources over the smoothed density field at $z = 0.45$. Contours are the same as in Fig. 8. Points have been colour-coded according to the best-fitting spectral template based on the optical photometry. Larger symbols indicate sources with higher NUV fluxes. The purple areas indicate regions where the concentration of NUV sources exceeds 3σ of the field average.

mass estimates from the cluster dynamics and weak lensing might be overestimated by the presence of substructures along the line of sight. Both hypotheses are plausible given the complex optical morphology of this cluster.

The total rest-frame *i*-band luminosity for this system within 1.22 Mpc (R_{200} as reported by Lu et al. 2010) is $L = 2.72 \pm 0.12 \times 10^{12}$ L$_{\odot}$, which implies a mass-to-light ratio of $M/L = 125 \pm 46$ M$_{\odot}$/L$_{\odot}$.

We also estimate the mass from optical traces using the Reyes et al. (2008) procedure. The centre of this object is taken from our group detection algorithm, but it is only 30 arcsec ($\sim$170 kpc) away from the brightest cluster galaxy.

We obtain the following parameters: $N_{200} = 40.7 \pm 2.1$ galaxies, $R_{200}^{\rm gal} = 1.44$ Mpc, which corrects the richness to $N_{200} = 54 \pm 4$, finally yielding a mass of $M_{200}^{N_{200}} = 6.4_{-1.9}^{+2} \times 10^{14}$ M$_{\odot}$, somewhat higher than the Lu et al. (2010) estimate from weak lensing and dynamics but well within the combined error bars.

We have at the moment few redshifts for this object, so we cannot improve the Lu et al. (2010) analysis, however we find a secondary (albeit with low significance) peak at $z \sim 0.45$ (see Fig. 13) that may indicate a complex system. Lu et al. (2010), with a larger sample, do not report the lower redshift feature, although they targeted red galaxies preferentially. The redshift distribution of the associated large structure shows, however, a bimodal distribution with one peak at $z \sim 0.45$ and another at $z \sim 0.47$. It is possible that we are observing a superposition of structures in this field.

7.3 NE Clump

This object has not previously been reported by studies of this field, although density and weak lensing maps by Lu et al. (2010) show detection of this structure. We confirm spectroscopically that it is at a similar redshift with $\langle z \rangle = 0.456$ and thus likely belongs to the large-scale structure associated with RX J1347. It forms, however, a sparse association without a clearly defined centre. Many bright red galaxies are associated with this structure.

The redshift distribution from the 11 available spectra for this system is quite broad, indicating that it may be still in the process of assembling (see Fig. 13). Using the biweight gapper algorithm of Beers, Flynn & Gebhardt (1990) (with bootstrapping), we obtain a velocity dispersion of $\sigma = 1260 \pm 260$ km s^{-1}, which would indicate a mass of $M_{200} \approx 1.9 \times 10^{15}$ M$_{\odot}$ following the Girardi et al. (1998) formula (corrected for the adopted cosmology). This mass estimate would make this system almost as massive as the central cluster and is surely a gross overestimate. The redshift distribution of the associated large structure is also very broad, but in contrast to LCDCS 0825 does not show a secondary peak at $z = 0.47$. Instead, it appears centred at $z \sim 0.45$ with an extended tail towards larger redshifts.

We also use the optical mass estimates, with the centre taken from our group detection algorithm, obtaining $N_{200} = 14.9 \pm 01.3$ galaxies, $R_{200}^{\rm gal} = 1.12$ Mpc, a corrected richness of $N_{200} = 20.5 \pm 4$ and an optical mass of $M_{200}^{N_{200}} = 2.1_{-1}^{+1.1} \times 10^{14}$ M$_{\odot}$, which is likely
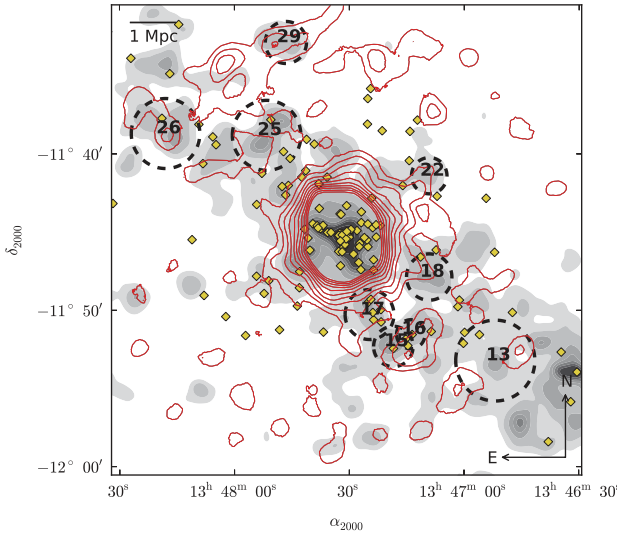
Figure 12. *XMM–Newton* X-ray significance contours (red) superimposed on the smooth galaxy density field (grey-scale). The first X-ray contour starts at 1σ per resolution element (32 arcsec × 32 arcsec) and contours are linearly spaced unti 10σ. The circles show the position of the optical group candidates where we performed the measurements. The numbers mark the group IDs. Small dots show the position of spectroscopic member galaxies.

closer to the real value and concordant with the upper limits for the X-ray luminosity (see Section 2.4).

7.3.1 LCDCS 0836

This object is a small, compact and isolated association of galaxies at $z_{phot} = 0.45$. No spectroscopic redshifts are available for this object.

7.3.2 BGV 2006–042

This source was detected as a candidate cluster by Barkhouse et al. (2006) in their serendipitous X-ray cluster search using *Chandra* archive observations. Its position coincides with a possibly infalling bright elliptical galaxy located in the middle of a filament extending towards the south-west. Five spectroscopic members are closely associated with this system (groups 15 and 16) with a median redshift of $z = 0.4502$.

7.4 Blue-fraction profiles for individual clusters

In Fig. 14 we plot the density profile and blue fractions for the three clusters presented in the field (RX J1347, LCDCS 0825 and the NE Clump). These quantities have been calculated in radial bins of 200 kpc centred on the clusters. Error bars are shown only for the blue fraction and are obtained from the statistics of individual measurements of the 100 Monte Carlo catalogues.

The blue-fraction profile for RX J1347 is apparently smoother than for the other clusters, which seem to 'jump' from low to high fractions in just one bin of radius. This may, however, be a statistical artefact given the fixed bins used and the limited number of members for the lower mass systems. In fact, the radius at which LCDCS 0825 and the NE Clump reach a relatively constant value is around $R \sim 0.3R_{200}^{gal}$, which is also similar in RX J1347. This radius is much lower than found in other studies, typically $R \sim$
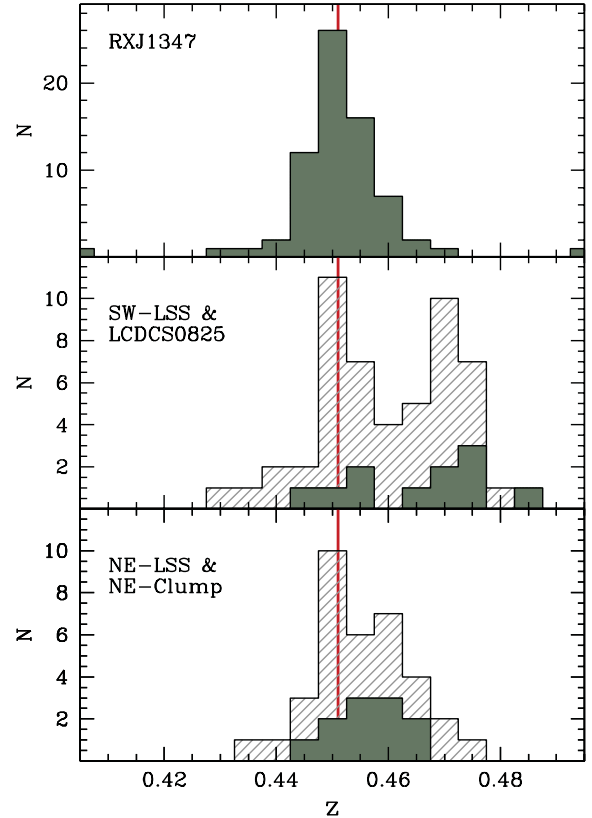

Figure 13. Spectroscopic redshift distribution for some structures in the field: Solid filled histograms show the redshift distribution for RX J1347, LCDCS 0825 and the NE Clump respectively. The hashed histograms display the redshift distributions for the associated large-scale structures. The vertical line marks $z = 0.45$.

1–$2R_{200}$ (e.g. Ellingson et al. 2001; Andreon et al. 2006; Verdugo et al. 2008).

First, it is important to note that we are referring to R_{200}^{gal}, which is typically larger than R_{200} (2.9 Mpc versus 2.3 Mpc for RX J1347). Secondly, we are using a photometrically selected sample, reaching fainter magnitudes than typical spectroscopic studies. As shown in Section 8, less luminous galaxies start to change their properties at higher densities than brighter ones; thus these trends are affected by this behaviour as faint galaxies dominate the number counts.

Differences in the radial trends of galaxy population for individual clusters have however been detected before (e.g. Verdugo et al. 2008; Mahajan et al. 2010) and may be related to the large-scale structure, dynamical properties or nature of the intracluster medium (Urquhart et al. 2010).

The density profiles for each cluster are provided to highlight the colour–density relation for these individual objects. Note the difference in the central density for each object, which also tends to be lower in the lower mass systems.

8 THE CLUSTER ENVIRONMENT AND GALAXY EVOLUTION

8.1 Blue fraction versus environment

To quantify further the dependence of the galaxy mix on environment, we plot in Fig. 15 the fraction of blue galaxies (F_{blue}) versus galaxy density (Σ_{10}) calculated in each of the 100
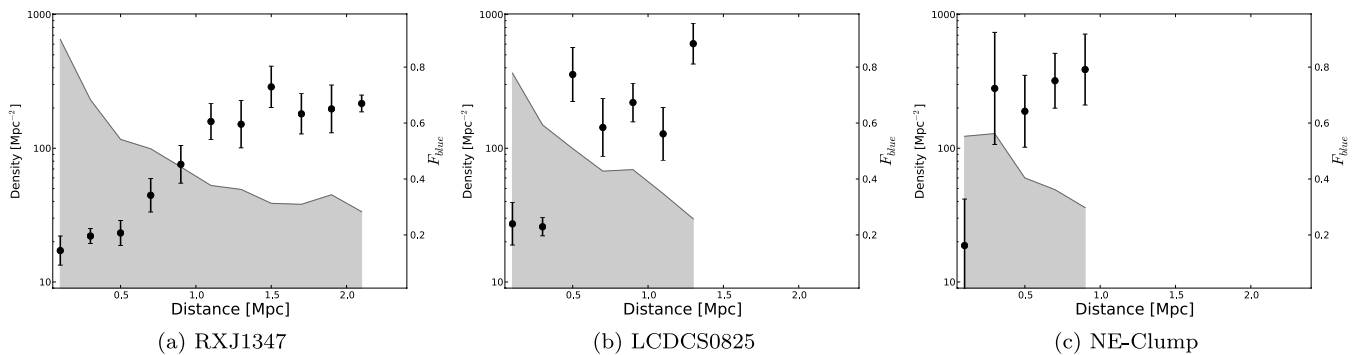
Figure 14. Blue-fraction profiles for RX J1347, LCDCS 0825 and the NE Clump in bins of 200 kpc out to a distance of $R = 1 R_{200}^{gal}$. The shaded areas in the background show the density profile calculated in rings of the same size. Note the large difference in central densities and differences in the blue-fraction profile.
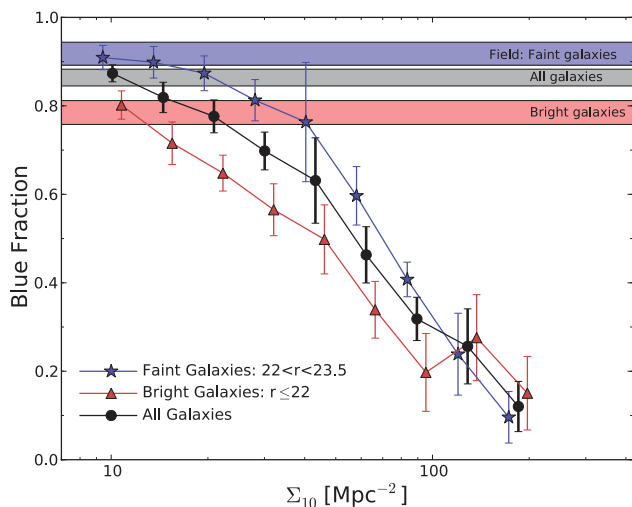

Figure 15. Fraction of blue galaxies as a function of the galaxy number density, for all galaxies (black circles), faint galaxies (blue stars) and bright galaxies (red triangles) as indicated in the figure. The horizontal regions mark the field fraction for the same magnitude cuts, obtained by averaging the four CFHTLS–Deep fields (Coupon et al. 2009).

Deep fields from the publicly available catalogues of Coupon et al. (2009) (see Section 8.2.1).

We also constructed a map of the distribution of galaxy types traced by the fraction of blue galaxies, using a similar method to that for the density map, i.e. for each point in a grid we instead calculate the fraction of blue galaxies using the 10th nearest neighbours. As in the density map, this procedure is performed for each of the 100 randomly drawn catalogues and averaged afterwards. This map is presented in Fig. 10. Comparing it with the density map (Fig. 8), it is possible to visualize the relation with environment: regions with a higher fraction of red galaxies tend to be located in denser environments. Despite this clear trend, the map allows us to appreciate the complexities of the relationship between galaxy mix and environment. There are few regions with a low fraction of red galaxies without the corresponding increase in density. The opposite also holds true: a few dense regions contain a high fraction of blue galaxies.

Similar maps, of either the fraction of blue galaxies or the mean colour, have been shown by e.g. Haines et al. (2006b) for the Shapley supercluster ($z = 0.05$), Schirmer et al. (2011) for the supercluster SCL 2243−0935 at $z = 0.45$ and Fassbender et al. (2008) for a cluster complex at $z = 0.95$. All these works have highlighted the complexities of the distribution of galaxy types against mean galaxy density over large scales.

8.2 Star-formation activity around RX J1347

We also quantify the distribution of the star-forming population by comparing the fraction of *GALEX* NUV sources as a function of galaxy number density. The results are presented in Fig. 16. Due to the smaller sample, we are unable to cover the same range of densities as in the case of the general blue population. The decline of the fraction of star-forming galaxies is a factor of 2 between $10 \, \text{Mpc}^{-2}$ and $80 \, \text{Mpc}^{-2}$, which is similar for the blue fraction.

Comparing the number of the unobscured starbursts detected by *GALEX* with the general blue population, we find that this fraction is similar across the full range of densities traced here. It is also similar to to the fraction found for the COSMOS field (see more in Section 8.2.1). The large error bars in the highest density bin are an indication of the very low number of star-forming galaxies found in the central regions of clusters. This result indicates that the *GALEX* NUV sources at our flux limits are a constant fraction of the blue population.

To test whether the properties of the star-forming population change with environment, we calculate the rest-frame UV

background-subtracted catalogue. We calculated this statistic in logarithmic spaced bins and weighted it by the total number of sources in each bin. Errors bars are the 1σ standard deviation weighted in a similar manner.

The decline of F_{blue} towards higher densities found by many authors (e.g. Kodama et al. 2001; Pimbblet et al. 2002; Tanaka et al. 2005) is also clearly appreciable around RX J1347. At low densities almost 90 per cent of the galaxies are blue, whereas in the highest density bin only 10 per cent are part of the blue population.

We next explore the dependence of this behaviour with luminosity, so we split the sample into bright ($r < 22$ mag) and faint ($22 \leq r < 23.5$ mag) galaxies. These two populations display somewhat distinct behaviour. The blue fraction in the bright galaxy population displays a steady decline with increasing galaxy density, reaching a saturation point at $\Sigma_{10} \approx 100 \, \text{Mpc}^{-2}$. On the other hand, F_{blue} for fainter galaxies shows a slow decline until $\Sigma_{10} \approx 40 \, \text{Mpc}^{-2}$, after which it starts to decrease at a faster pace.

The fraction of blue galaxies in the lowest density bin is compatible with the values found for the field population. They are calculated using the same redshifts and magnitude cuts in the CFHTLS–
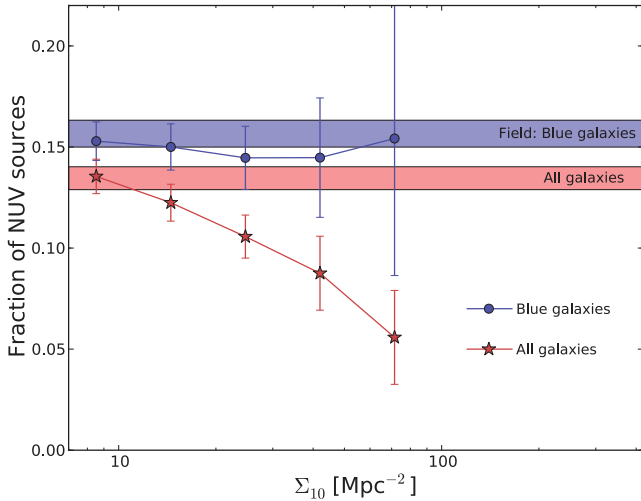
Figure 16. Fraction of detected *GALEX* NUV sources compared with all galaxies and only blue ones, plotted as a function of galaxy number density. The number of strong starbursts detected by GALEX decreases towards the high-density regions, but they represent a constant fraction of the blue population. The field fraction obtained for the COSMOS field is shown by the horizontal regions.

luminosity function in three environments: a low-density environment with $\Sigma_{10} < 20\,\mathrm{Mpc}^{-2}$, a medium-density environment with $20 \leq \Sigma_{10} < 40\,\mathrm{Mpc}^{-2}$ and a high-density environment with $\Sigma_{10} \geq 40\,\mathrm{Mpc}^{-2}$.

Absolute magnitudes were calculated directly from the apparent NUV magnitudes without applying *k*-corrections. As the *GALEX* NUV filter at $z = 0.45$ has $\lambda_{\mathrm{eff}} \approx 1500\,\mathrm{\AA}$ (similar to the rest-frame FUV filter), we expect that the introduced errors are small.

The luminosity functions are plotted in Fig. 17, together with the best-fitting Schechter function (Schechter 1976, equation 2) obtained from a χ^2 minimization algorithm. The inset shows the 1σ confidence limits. The results for the characteristic magnitude $M^\star_{\mathrm{UV}}$ and the faint-end slope α are the following:

(i) low density: $M^\star_{\mathrm{UV}} = -19.47 \pm 0.24$, $\alpha = -0.77 \pm 0.29$;
(ii) medium density: $M^\star_{\mathrm{UV}} = -19.46 \pm 0.45$, $\alpha = -0.65 \pm 0.50$;
(iii) high density: $M^\star_{\mathrm{UV}} = -19.33 \pm 0.93$, $\alpha = -0.43 \pm 1.25$.

The values of $M^\star_{\mathrm{UV}}$ are about 1.3 mag brighter than in $z \sim 0$ clusters (e.g. Haines et al. 2011a), but consistent with field values at $z \sim 0.5$ (Arnouts et al. 2005). The faint-end slopes are, however, somewhat shallower in our case. This might be due to our relatively bright magnitude limit, which does not allow us to sample the faint end of the luminosity function adequately.

We also show in Fig. 17 the median $(g - r)$ colours for the star-forming population as a function of environment, together with the respective 25th and 75th percentiles of the distribution. The density bins are the same as in Fig. 16. The colours of the star-forming population are very similar across all galaxy densities.

Finally, we calculate the ultraviolet spectral slope β for NUV sources. This parameter has been shown to be sensitive to extinction in normal star-forming galaxies (e.g. Kong et al. 2004). We use the *u*-band and NUV magnitudes ($\lambda_{\mathrm{eff}} \approx 1560$ and $2580\,\mathrm{\AA}$ at $z = 0.45$ respectively) and a variation of the formula of Kong et al. (2004) for local galaxies:

$$\beta = \frac{\log(f_{\mathrm{NUV}}) - \log(f_u)}{\log(\lambda_{\mathrm{NUV}}) - \log(\lambda_u)}, \tag{6}$$

where λ_{NUV} and λ_u are the respective effective wavelengths for those bands.

The median of the values as a function of galaxy density is shown in the middle of the right panel of Fig. 17, together with the 25th and 75th percentiles of the distribution. These values are typical for UV-selected star-forming galaxies (Schiminovich et al. 2005) and do not differ much with population in low redshift clusters (Haines et al. 2011b). They imply typical extinctions in range $0.5 < A_{\mathrm{UV}} < 2.5$ mag at $\lambda = 1500\,\mathrm{\AA}$ for 50 per cent of the sample, with a median of $A_{\mathrm{UV}} \sim 1.5$ mag. These values are also almost independent of environment.

A slight increase of the extinction is detected at intermediate densities (the top 75th percentile), however it is still within the expectations for the star forming population.

These tests show that the star-forming population across the supercluster environment is notably homogeneous and only their relative abundance decreases with increasing density. This argues against a slow decline of star formation with environment and favours a rapid change between galaxy types, as transition objects appear to be statistically insignificant from the UV perspective.

It is possible, however, that the transformation is hidden by dust as some studies suggest (e.g. Wolf et al. 2009). In that case, the nature of the star formation should be different from that in normal galaxies, probably more centrally concentrated, making it difficult to probe the UV emission due to the larger dust columns (Geach et al. 2009). However, this transition of star-formation mode should also occur on short time-scales, otherwise we would detect it as either reddening in the colour distribution of NUV sources, dimming in the NUV luminosity function or a change in the UV spectral slopes.

In Fig. 11 we show the distribution of the NUV emitters. They are sparsely distributed, with very few obvious concentrations; some of these concentration are coincident with detected group candidates. When we construct the density map of NUV sources, using the same method described in Section 8, additional concentrations become appreciable. This is due to the different probabilities for individual galaxies assigned during the statistical background subtraction. We plot only concentrations with at least 3σ significance over the mean of the field. It is interesting to note that some of these concentrations are coincident with the large-scale structure and candidate galaxy groups. In particular, the cluster LCDCS 0825 features a relatively large population of star-forming galaxies.

8.2.1 Comparison with the general field population

Our investigation is focused on the galaxy properties in the large-scale structures around RX J1347. However, the lowest density bin traced in Figs 15 and 16 can be considered as representative of the field population, as its density is lower than the mean of the CFHTLS fields. To test this and to provide proper comparison with the general field population, we use available data from current large-area surveys.

In the case of Fig. 15 we used the latest public reduction of the CFHTLS–Deep fields (Coupon et al. 2009), which provides accurate photometric redshifts using a very similar methodology to our study. We use the same photometric redshifts and magnitude cuts as in our case. Since the CFHTLS–Deep fields are deeper than the data used in our investigation, their photo-*z* are also more accurate, however we do not expect that this introduces any bias, as the effects of contamination from different redshift bins should be averaged out. In fact, it is reassuring that the blue fraction averaged for the four fields is very similar to the one measured in our lowest density bin, as can be seen in Fig. 15.
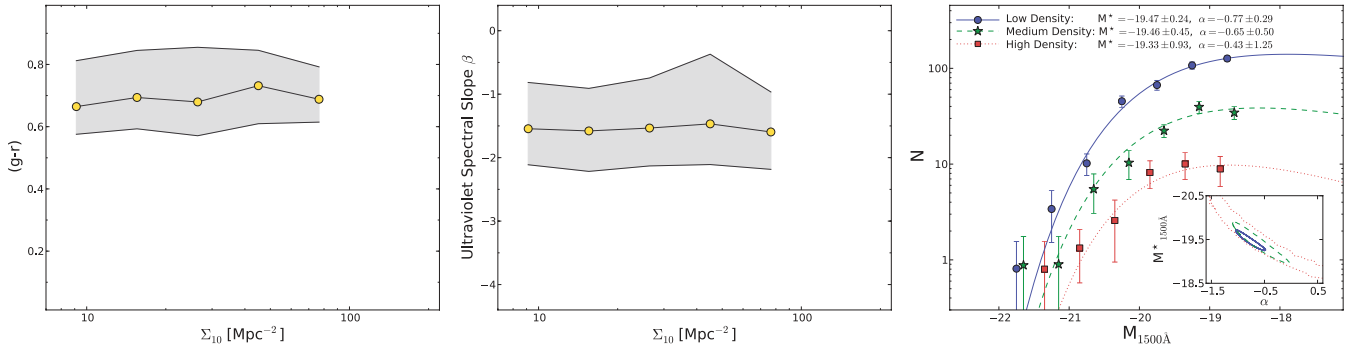
Figure 17. Properties of the NUV emitters as a function of environment. Left: the median $(g - r)$ colour. Middle: the median of the extinction-sensitive ultraviolet spectral slope β. In both cases, the lower and upper lines that enclose the shaded areas represent the 25th and 75th percentiles of the distribution respectively. Right: rest-frame UV (1450 Å) luminosity function for the *GALEX* sources in three different environments. The lines show the best-fitting Schechter functions for three different environments: low with $\Sigma_{10} < 20\,\mathrm{Mpc}^{-2}$, medium with $20 \leq \Sigma_{10} < 40\,\mathrm{Mpc}^{-2}$ and high-density with $\Sigma_{10} \geq 40\,\mathrm{Mpc}^{-2}$. The inset displays the 1σ uncertainty for α and $M^{\star}_{\mathrm{UV}}$ parameters.

In the case of the NUV fraction comparison, we use data taken as part of the COSMOS survey centred on the CFHTLS–D2 field. Deep *GALEX* data have been taken over $2 \times 2\,\mathrm{deg}^2$ on this field (PI: Schiminovich) as part of the Deep Imaging Survey (DIS) and advanced data products have been made available (e.g. Zamojski et al. 2007). However, to make our study fully comparable, we prefer to use the data from the COSMOS_00 stack, which is the shallowest stack available at MAST in this field. The total exposure time in the NUV band is 8128 s, similar to the data we are using for the cluster. We also use the catalogues produced by the *GALEX* pipeline. We then match the CFHTLS–D2 field (in which the COSMOS field is centred) using the same procedure as described in 2.3. NUV fractions are then calculated relative to the total population and the blue one. As in the previous case, the general field star-forming fractions are very similar to those calculated for the lowest density bin.

8.3 Galaxy properties in groups near clusters

In Fig. 9 we have plotted the distribution of the groups detected by the Voronoi–Delaunay technique (Section 5.2). Blue fractions have been calculated within an aperture given by the radius R_{group} for each group for each of the individual 100 Monte Carlo catalogues. We consider 'red groups', those with $F_{\mathrm{blue}} < 0.5$; 'green groups', those with $0.5 < F_{\mathrm{blue}} < 0.75$ and 'blue groups', with $F_{\mathrm{blue}} > 0.75$. We have marked them with the corresponding colour in Fig. 9. With some exceptions, we note that more evolved groups are located in the large-scale structure and tend to be closer to larger overdensities.

To test how the evolutionary status of galaxies depends on the environmental conditions within each group, we plot in Fig. 18 the fraction of blue galaxies as a function of the mean galaxy density for each group. Despite the large scatter, a trend is observed in which denser groups (and clusters) have lower F_{blue}. However, we do find few relatively dense groups (25–30 Mpc^{-2} with high F_{blue}). Most of these groups are located at the south-west extreme of the large-scale structure (see Fig. 9). A number of groups with similar mean densities contain very low F_{blue}, at the same level as the very massive central cluster.

Note that the fraction of blue galaxies for RX J1347 is within our expectations from the Butcher–Oemler effect for clusters at those redshifts (e.g. Ellingson et al. 2001; Zenteno et al. 2011).

Comparing F_{blue} with the total rest-frame *i*-band luminosity for each group results in a similarly noisy correlation. More luminous
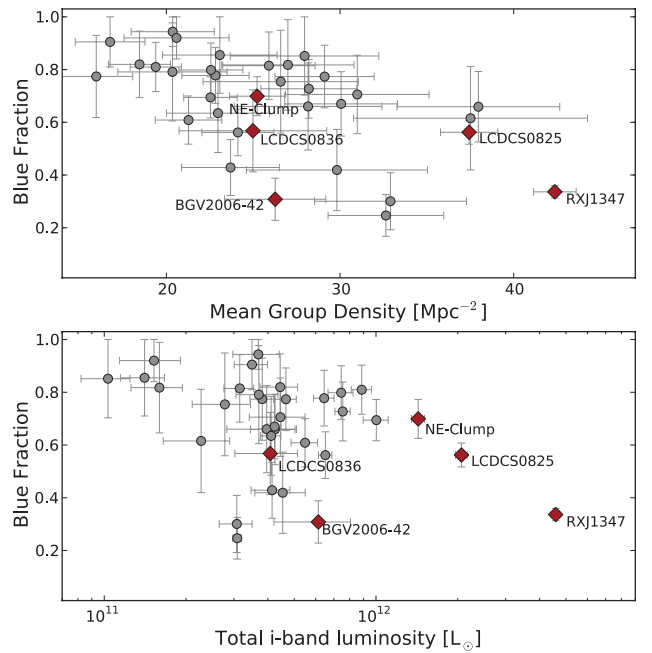

Figure 18. Fraction of blue galaxies versus the mean group density and rest-frame *i*-band luminosity for each group. Error bars are the 1σ standard deviations obtained from the 100 Monte Carlo catalogues. Previously detected groups and clusters are marked by red diamonds and individual identifications. Note the large scatter in galaxy content for groups with similar properties.

systems indeed have lower F_{blue}, whereas fainter ones have high fractions. In between, a high dispersion can be noted, including some relatively faint groups with a very low fraction of blue galaxies.

Although it is difficult to assess the reality of these galaxy associations, as well as their dynamical state, from photometry alone, we find these trends interesting as the evolutionary state of groups may have a stronger impact on their galaxy content than their total masses.

We finally test the overall impact of groups in the colour–density relation (Fig. 15). For that we separate galaxies according to their membership. Cluster galaxies are those belonging to the three clusters in our field (namely RX J1347, LCDCS 0825 and the NE Clump). Group galaxies are those belonging to groups detected
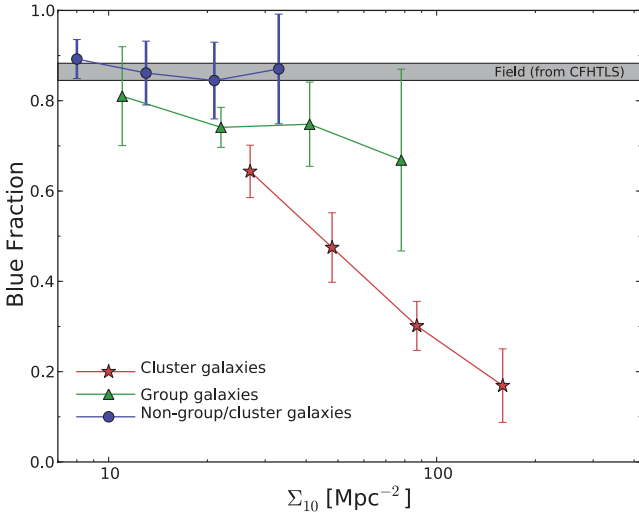
Figure 19. Blue fraction as a function of galaxy density split according to galaxy membership: clusters, groups or none. Notice the weaker trends for non-cluster galaxies.

by the Voronoi technique. We include in each case all galaxies within twice the radius obtained from the group detection algorithm ($R_{\rm group}$. This means that groups within twice the radius of the clusters are excluded to avoid duplicity. Similarly, we checked for duplicated galaxies in the composite group catalogue and eliminated them. We also created a catalogue with galaxies that do not belong to either category to check the impact of the smooth density field in their properties.

Results are plotted in Fig. 19, where the fraction of blue galaxies versus galaxy density is displayed. Galaxies with no membership have a rather large blue population over a relatively large range of densities, similar to the general field. Galaxies belonging to groups display a rather modest change in $F_{\rm blue}$ albeit with a large scatter. On the other hand, clusters exhibit a very strong change of $F_{\rm blue}$ with density, indicating that they are very effective in transforming galaxies from one type into another. This also means that the bulk of the environmental signal in the colour–density relation (cf. Fig. 15) is likely due to these massive systems.

This does not mean that groups are not places of galaxy transformation. In fact, Fig. 18 shows a large range of properties of group candidates; however, it is possible that the mechanisms acting in such places are different from those in clusters and not necessarily related to the galaxy density. Furthermore, it is important to note that the diversity of group properties (as well as contamination effects) may wash out some of the environmental signal.

This result is similar to those of Li et al. (2009), where a large number of *photometrically* selected groups around intermediate redshift clusters were analysed. They find that the environmental signal is weaker outside the virial radius of clusters. It is, however, in contradiction with studies at low redshift, where the environmental variation of the galaxy population is similar regardless of the mass of the system (Lewis et al. 2002; Balogh et al. 2004).

8.4 Evolution along the large-scale structure

We now test the evolution of galaxies along the large-scale structure measured using an oblique area as indicated in Fig. 9. We trace the environment in this case using the position relative to the south-west corner. This may blur out the effect of small groups, but may enhance any effect purely related to the large-scale structure.
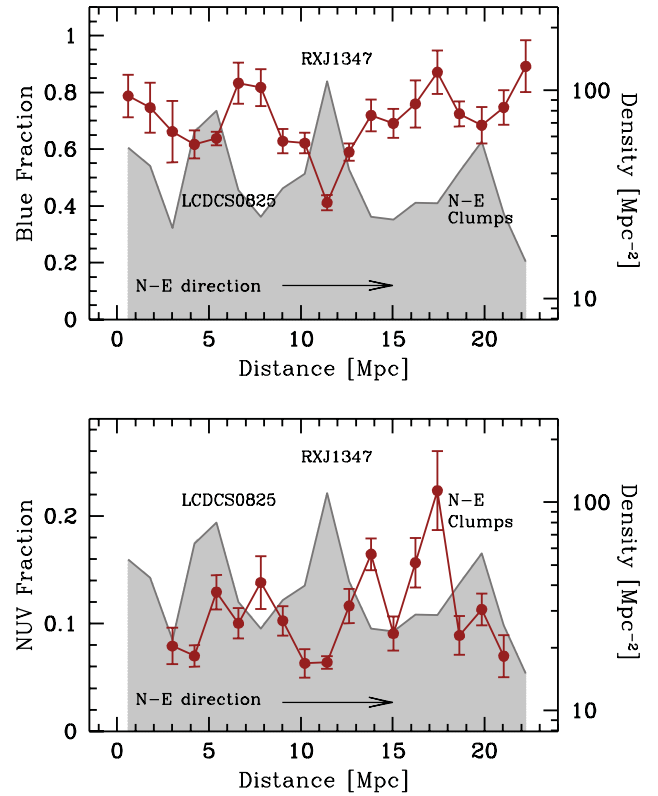

Figure 20. Fraction of blue galaxies (top) and *GALEX* NUV sources (bottom) as a function of position within the large-scale structure (red points). The origin is taken from the south-west corner (see Fig. 9). In the background, we plot in grey the mean galaxy density of the large-scale structure. The peaks associated with the main clusters are clearly discernible and marked to guide the eye. A density enhancement is also observed in the south-west extreme of the large-scale structure.

We calculate the fraction of blue galaxies and *GALEX* NUV sources as a function of distance. The results are shown in Fig. 20. We plot in the background the mean galaxy density, to appreciate its change along the large scale structure (LSS). The highest peaks associated with RX J1347, LCDCS 0825 and the NE Clump are evident. We note in the plot the change of blue fraction and how it increases when the galaxy density decreases. In particular, we note the low fraction of blue galaxies associated with the position of RX J1347, despite the contamination of galaxies at larger radii.

The colour–density relation is somewhat broken at the south-west extreme of the large-scale structure, where few dense blue-dominated groups are located. The mean density increases at that point and so does the blue fraction.

Similar increases of star-formation activity with density have mainly been reported at high redshifts (Elbaz et al. 2007; Tran et al. 2010) or in particular environments like galaxy pairs (Ellison et al. 2008; Wong et al. 2011), but not often in groups at lower redshifts. We will wait for the results of our spectroscopic observations to make a complete assessment of the properties of these systems.

The fraction of *GALEX* NUV sources follows a similar trend with distance, albeit noisier due to the lower number of available sources. However, these large variations may also indicate places where the star formation is locally enhanced or suppressed depending on the local physical conditions. Unfortunately the *GALEX* observations do not cover the region of the previously mentioned blue-dominated groups.

9 DISCUSSION

The study of the effects of large-scale structure around clusters has recently been a matter of intense research. This is motivated by the evidence that galaxy transformations start at large clustercentric radii (Rines et al. 2005; Porter & Raychaudhury 2007; Verdugo et al. 2008). As simulations in ΛCDM cosmologies predict that matter is accreted into rich clusters through filaments and infalling smaller systems (e.g. Bond, Kofman & Pogosyan 1996; Suhhonenko et al. 2011), these regions are expected to have an increase of interactions that might explain the origin of the cluster population dichotomy.

In the local Universe, Mercurio et al. (2006) and Haines et al. 2006a have studied the optical properties of galaxies inhabiting the Shapley supercluster ($z = 0.05$). They have shown that the environmental dependence of the global galaxy luminosity function is mostly driven by the change of the galaxy mix (colour–density relation). The luminosity function for blue galaxies is similar for all environments. Similar results were reported by Gavazzi et al. (2010) for galaxies belonging to the Coma supercluster.

In subsequent works, Haines et al. (2011a,b) have completed a census of the star formation around the Shapley supercluster using *GALEX* UV and *Spitzer* mid-infrared observations. They found that the respective luminosity functions for cluster star-forming galaxies do not differ significantly from the comparison fields. Bai et al. (2009) and Biviano et al. (2011) have also found similar behaviour.

Using a very large catalogue of optically selected clusters, Hansen et al. (2009) have also provided evidence of the very homogeneous nature of the blue population, which depends little on system mass or clustercentric distance. This has also been confirmed by spectroscopic studies of intermediate-redshift clusters. For example, Poggianti et al. (2008) and Verdugo et al. (2008) have found that the mean strengths of emission lines ([O II] and Hα) for the *star-forming* population show no dependence on environment.

Furthermore, detailed kinematical studies of spiral galaxies in distant clusters ($z = 0.3$–0.5) have failed to find important differences in their velocity fields compared with the field population (Kutdemir et al. 2010). Larger samples are, however, needed to probe this in more detail.

In this paper, we have shown that UV-selected star-forming galaxies have similar properties at $z \sim 0.5$, regardless of their position in the large-scale structure (Fig. 17). Furthermore, we provide evidence that the cluster environment plays a fundamental role in shaping their own galaxy populations and trends due to less massive galaxy systems being much weaker (Fig. 19, see also Li et al. 2009).

Probably the most viable transformation process to explain the homogeneity of the active population with environment and its rapid transformation in massive systems is ram-pressure stripping (e.g. Fujita 2004). This mechanism provides the necessary time-scales to make the transition between galaxy types fast enough that one cannot easily detect transition galaxy types.

Recent simulations (e.g. Book & Benson 2010; Tecce, Cora & Tissera 2011) have shown that the effects of ram-pressure stripping are able to reproduce the star-formation profiles in clusters out to large clustercentric distances. In the models of Tecce et al. (2011), the fraction of galaxies with cold gas within R_{200} depends on both cluster mass and redshift. The predicted fraction at $z = 0$ is very low for clusters with masses $M_{200} > 10^{14}\,M_{\odot}$ and much higher for clusters with smaller masses. Interestingly, the relation between the blue fraction within R_{200} and cluster mass found by Hansen et al. (2009) at $z \approx 0$ remains almost flat for clusters with masses $M_{200} > 10^{14}\,M_{\odot}$ and changes rapidly below that point, indicating a change

in the effectiveness of the transformation processes at that mass threshold in concordance with previous simulations.

Regarding the effects of large-scale structure in the galaxy population, we have shown that galaxy groups have a large diversity in their galaxy content (Fig. 18), with little dependence on their global galaxy density or total stellar mass content. This might be a sign that other effects, perhaps related to their dynamical state, alter the overall trends.

Finally, we should stress that we have found no evidence of enhanced star-formation activity in the LSS as recent works have claimed (Braglia et al. 2007; Marcillac et al. 2007; Fadda et al. 2008; Porter et al. 2008). Instead we find regions with larger fractions of blue and/or star-forming galaxies at moderate densities, indicating that some preprocessing is occurring in the large-scale structure. Such pockets of concentrated but rather normal star formation have also been recently found around Cl 0016+16 ($z = 0.55$) by Geach et al. (2011a).

Tran et al. (2009), however, have found a clear increase of the star-formation activity around a super group at $z \sim 0.4$. Whether such groups are abundant at intermediate redshifts is unclear. If such systems exist around RX J1347, it might be possible that our optical–UV study is missing them due to the effects of dust attenuation. However, as has been argued before, we should be able to detect the change of star-formation mode (unobscured to obscured) if it occurs over relatively long time-scales and is caused by environmental effects.

10 SUMMARY AND PROSPECTS

We have presented a study on the large-scale structures around the most luminous X-ray cluster RX J1347.5−1145. As expected from large-scale growth theory, we have found that RX J1347, one of the most massive known galaxy clusters, is embedded in a rich filamentary network that extends for at least 20 Mpc. We have identified a number of galaxy groups in the filaments, which are likely to be accreted by the main cluster at later times. Two other massive systems are associated with the large-scale structure, making RX J1347 a good candidate for a supercluster.

We calculated the fraction of blue galaxies as a function of environment characterized by the local galaxy density. Similarly to other studies, we confirm the low number of blue galaxies in high-density regions. This fraction drops from ∼85 per cent in the low-density environment to ∼10 per cent at the highest densities in the cluster cores. This relation is also luminosity (mass) dependent.

The relationship of the galaxy population to environment is also studied by using 9-ks *GALEX* NUV exposures, which trace the unobscured star-forming population. As a function of environment, its fraction follows the colour–density relation closely. The properties of the star-forming population are also remarkably similar for all environments. We interpret this as evidence of a rapid transformation of galaxy types.

This is further confirmed when we analyse different environments independently. We find that the cluster environment carries most of the signal of the colour–density relation. Galaxy group candidates, however, display a large variation in their properties, a signal that some transformations are also occurring in these environments, but this might not be directly related to galaxy density.

Our results are compatible with a scenario of rapid suppression of star-formation activity in the vicinity of clusters, likely due to specific processes. Preprocessing is also occurring in the large-scale structure but its nature is apparently heterogeneous and probably depends on particular conditions.

The recently completed VIMOS campaign (30 h) over a full 1 deg^2 will allow us to confirm the trends studied here, via additional star-formation indicators. We can identify optical active galactic nuclei and assess the properties of passive galaxies by using strong absorption lines. We should also be able to verify and investigate the properties of groups and clusters identified in this study (mostly) by photometric means.

REFERENCES

Andreon S., Quintana H., Tajer M., Galaz G., Surdej J., 2006, MNRAS, 365, 915

Arnouts S. et al., 2005, ApJ, 619, L43

Bai L., Rieke G. H., Rieke M. J., Christlein D., Zabludoff A. I., 2009, ApJ, 693, 1840

Baldry I. K., Balogh M. L., Bower R. G., Glazebrook K., Nichol R. C., Bamford S. P., Budavari T., 2006, MNRAS, 373, 469

Balogh M. L., Morris S. L., Yee H. K. C., Carlberg R. G., Ellingson E., 1999, ApJ, 527, 54

Balogh M. et al., 2004, MNRAS, 348, 1355

Barkhouse W. A. et al., 2006, ApJ, 645, 955

Bauer A. E., Grützbauch R., Jørgensen I., Varela J., Bergmann M., 2011, MNRAS, 411, 2009

Baum W. A., 1959, PASP, 71, 106

Beers T. C., Flynn K., Gebhardt K., 1990, AJ, 100, 32

Bender R. et al., 2001, in Cristinia S., Renzini A., Williams R. E., eds, ESO Astrophys. Symp., Globular Clusters – Guides to Galaxies. Springer-Verlag, Heidelberg, p. 96 (doi: 10.1007/10854354_18)

Benítez N., 2000, ApJ, 536, 571

Bertin E., Arnouts S., 1996, A&AS, 117, 393

Bielby R. M. et al., 2010, A&A, 523, 66

Biviano A., Fadda D., Durret F., Edwards L. O. V., Marleau F., 2011, A&A, 532, A77

Böhringer H. et al., 2000, ApJS, 129, 435

Böhringer H. et al., 2001, A&A, 369, 826

Böhringer H. et al., 2004, A&A, 425, 367

Bond J. R., Kofman L., Pogosyan D., 1996, Nat, 380, 603

Book L. G., Benson A. J., 2010, ApJ, 716, 810

Bradač M. et al., 2005, A&A, 437, 49

Bradač M. et al., 2008, ApJ, 681, 187

Braglia F., Pierini D., Böhringer H., 2007, A&A, 470, 425

Braglia F. G., Pierini D., Biviano A., Böhringer H., 2009, A&A, 500, 947

Butcher H., Oemler A., Jr, 1978, ApJ, 226, 559

Chilingarian I. V., Melchior A.-L., Zolotukhin I. Y., 2010, MNRAS, 405, 1409

Christlein D., Zabludoff A. I., 2005, ApJ, 621, 201

Cohen J. G., Kneib J.-P., 2002, ApJ, 573, 524

Coupon J. et al., 2009, A&A, 500, 981

Dressler A., 1980, ApJ, 236, 351

Dressler A., Thompson I. B., Shectman S. A., 1985, ApJ, 288, 481

Elbaz D. et al., 2007, A&A, 468, 33

Ellingson E., Lin H., Yee H. K. C., Carlberg R. G., 2001, ApJ, 547, 609

Ellison S. L., Patton D. R., Simard L., McConnachie A. W., 2008, AJ, 135, 1877

Erben T. et al., 2009, A&A, 493, 1197

Ettori S., Allen S. W., Fabian A. C., 2001, MNRAS, 322, 187

Fadda D., Biviano A., Marleau F. R., Storrie-Lombardi L. J., Durret F., 2008, ApJ, 672, L9

Fassbender R., Böhringer H., Lamer G., Mullis C. R., Rosati P., Schwope A., Kohnert J., Santos J. S., 2008, A&A, 481, L73

Finn R. A. et al., 2010, ApJ, 720, 87

Finoguenov A. et al., 2010, MNRAS, 403, 2063

Fujita Y., 2004, PASJ, 56, 29

Gallazzi A. et al., 2009, ApJ, 690, 1883

Garilli B., Fumana M., Franzetti P., Paioro L., Scodeggio M., Le Fèvre O., Paltani S., Scaramella R., 2010, PASP, 122, 827

Gavazzi G., Fumagalli M., Cucciati O., Boselli A., 2010, A&A, 517, 73

Geach J. E., Smail I., Moran S. M., Treu T., Ellis R. S., 2009, ApJ, 691, 783

Geach J. E., Ellis R. S., Smail I., Rawle T. D., Moran S. M., 2011a, MNRAS, 413, 177

Geach J. E., Murphy D. N. A., Bower R. G., 2011b, MNRAS, 413, 3059

Girardi M., Giuricin G., Mardirossian F., Mezzetti M., Boschin W., 1998, ApJ, 505, 74

Girardi M., Manzato P., Mezzetti M., Giuricin G., Limboz F., 2002, ApJ, 569, 720

Gitti M., Schindler S., 2004, A&A, 427, L9

Gitti M., Ferrari C., Domainko W., Feretti L., Schindler S., 2007a, A&A, 470, L25

Gitti M., Piffaretti R., Schindler S., 2007b, A&A, 472, 383

Gladders M. D., Lopez-Cruz O., Yee H. K. C., Kodama T., 1998, ApJ, 501, 571

Gonzalez A. H., Zaritsky D., Dalcanton J. J., Nelson A., 2001, ApJS, 137, 117

Haines C. P., La Barbera F., Mercurio A., Merluzzi P., Busarello G., 2006a, ApJ, 647, L21

Haines C. P., Merluzzi P., Mercurio A., Gargiulo A., Krusanova N., Busarello G., La Barbera F., Capaccioli M., 2006b, MNRAS, 371, 55

Haines C. P. et al., 2009a, ApJ, 704, 126

Haines C. P., Smith G. P., Egami E., Okabe N., Takada M., Ellis R. S., Moran S. M., Umetsu K., 2009b, MNRAS, 396, 1297

Haines C. P., Busarello G., Merluzzi P., Smith R. J., Raychaudhury S., Mercurio A., Smith G. P., 2011a, MNRAS, 412, 127

Haines C. P., Busarello G., Merluzzi P., Smith R. J., Raychaudhury S., Mercurio A., Smith G. P., 2011b, MNRAS, 412, 145

Halkola A., Hildebrandt H., Schrabback T., Lombardi M., Bradač M., Erben T., Schneider P., Wuttke D., 2008, A&A, 481, 65

Hansen S. M., Sheldon E. S., Wechsler R. H., Koester B. P., 2009, ApJ, 699, 1333

Hicks A. K., Mushotzky R., Donahue M., 2010, ApJ, 719, 1844

Hildebrandt H., Pielorz J., Erben T., van Waerbeke L., Simon P., Capak P., 2009, A&A, 498, 725

Ilbert O. et al., 2006, A&A, 457, 841

Kiang T., 1966, Z. Astrophys., 64, 433

Kim R. S. J. et al., 2002, AJ, 123, 20

Kitayama T., Komatsu E., Ota N., Kuwabara T., Suto Y., Yoshikawa K., Hattori M., Matsuo H., 2004, PASJ, 56, 17

Kodama T., Smail I., Nakata F., Okamura S., Bower R. G., 2001, ApJ, 562, L9

Komatsu E. et al., 2001, PASJ, 53, 57

Kong X., Charlot S., Brinchmann J., Fall S. M., 2004, MNRAS, 349, 769

Koyama Y. et al., 2008, MNRAS, 391, 1758

Kutdemir E., Ziegler B. L., Peletier R. F., Da Rocha C., Böhm A., Verdugo M., 2010, A&A, 520, A109

Leauthaud A. et al., 2010, ApJ, 709, 97

Lerchster et al., 2011, MNRAS, 411, 2667

Lewis I. et al., 2002, MNRAS, 334, 673

Li I. H., Yee H. K. C., Ellingson E., 2009, ApJ, 698, 83

Loh Y.-S., Ellingson E., Yee H. K. C., Gilbank D. G., Gladders M. D., Barrientos L. F., 2008, ApJ, 680, 214

Lu T. et al., 2010, MNRAS, 403, 1787

Mahajan S., Haines C. P., Raychaudhury S., 2010, MNRAS, 404, 1745

Marcillac D., Rigby J. R., Rieke G. H., Kelly D. M., 2007, ApJ, 654, 825

Marinoni C., Davis M., Newman J. A., Coil A. L., 2002, ApJ, 580, 122

Mason B. S. et al., 2010, ApJ, 716, 739

Medezinski E., Broadhurst T., Umetsu K., Oguri M., Rephaeli Y., Benítez N., 2010, MNRAS, 405, 257

Mercurio A. et al., 2006, MNRAS, 368, 109

Moran S. M., Ellis R. S., Treu T., Smith G. P., Rich R. M., Smail I., 2007, ApJ, 671, 1503

Morrissey P. et al., 2007, ApJS, 173, 682

Ota N. et al., 2008, A&A, 491, 363

Pelló R. et al., 2009, A&A, 508, 1173

Pickles A. J., 1998, PASP, 110, 863

Pimbblet K. A., Smail I., Kodama T., Couch W. J., Edge A. C., Zabludoff A. I., O'Hely E., 2002, MNRAS, 331, 333

Poggianti B. M. et al., 2008, ApJ, 684, 888

Popesso P., Biviano A., Romaniello M., Böhringer H., 2007, A&A, 461, 411

Porter S. C., Raychaudhury S., 2007, MNRAS, 375, 1409

Porter S. C., Raychaudhury S., Pimbblet K. A., Drinkwater M. J., 2008, MNRAS, 388, 1152

Ramella M., Boschin W., Fadda D., Nonino M., 2001, A&A, 368, 776

Reyes R., Mandelbaum R., Hirata C., Bahcall N., Seljak U., 2008, MNRAS, 390, 1157

Rines K., Geller M. J., Kurtz M. J., Diaferio A., 2005, AJ, 130, 1482

Rudnick G. et al., 2009, ApJ, 700, 1559

Saintonge A., Tran K., Holden B. P., 2008, ApJ, 685, L113

Schechter P., 1976, ApJ, 203, 297

Schiminovich D. et al., 2005, ApJ, 619, L47

Schindler S. et al., 1995, A&A, 299, 9

Schindler S., Hattori M., Neumann D. M., Boehringer H., 1997, A&A, 317, 646

Schirmer M., Hildebrandt H., Kuijken K., Erben T., 2011, A&A, 532, 57

Schlegel D. J., Finkbeiner D. P., Davis M., 1998, ApJ, 500, 525

Scodeggio M. et al., 2005, PASP, 117, 1284

Suhhonenko I. et al., 2011, A&A, 531, 149

Tanaka M., Kodama T., Arimoto N., Okamura S., Umetsu K., Shimasaku K., Tanaka I., Yamada T., 2005, MNRAS, 362, 268

Tanaka M., Hoshi T., Kodama T., Kashikawa N., 2007, MNRAS, 379, 1546

Tanaka M., Finoguenov A., Kodama T., Koyama Y., Maughan B., Nakata F., 2009, A&A, 505, L9

Tecce T. E., Cora S. A., Tissera P. B., 2011, MNRAS, 416, 3170

Tran K., Saintonge A., Moustakas J., Bai L., Gonzalez A. H., Holden B. P., Zaritsky D., Kautsch S. J., 2009, ApJ, 705, 809

Tran K. et al., 2010, ApJ, 719, L126

Urquhart S. A., Willis J. P., Hoekstra H., Pierre M., 2010, MNRAS, 406, 368

Verdugo M., Ziegler B. L., Gerken B., 2008, A&A, 486, 9

von der Linden A., Wild V., Kauffmann G., White S. D. M., Weinmann S., 2010, MNRAS, 404, 1231

Wolf C. et al., 2009, MNRAS, 393, 1302

Wong K. C. et al., 2011, ApJ, 728, 119

Yee H. K. C., Ellingson E., Carlberg R. G., 1996, ApJS, 102, 269

Zamojski M. A. et al., 2007, ApJS, 172, 468

Zenteno A. et al., 2011, ApJ, 734, 3

Zhang Y., Finoguenov A., Böhringer H., Ikebe Y., Matsushita K., Schuecker P., 2004, A&A, 413, 49

Zhang Y., Böhringer H., Finoguenov A., Ikebe Y., Matsushita K., Guzzo L., Collins C. A., 2006, A&A, 456, 55

APPENDIX A: COMPARISON OF DENSITY ESTIMATES

We provide here two plots that compare estimates of the two measures of density. In the first plot (Fig. A1) two densities estimates are compared (Σ_5 and Σ_{10}) for all galaxies drawn from two randomly selected realizations of the 100 Monte Carlo realizations. The second plot (Fig. A2) shows the mean group density measured within the aperture R_{group} versus the median density Σ_5 and Σ_{10} for all galaxies within the same aperture.

APPENDIX B: TABLES WITH PROPERTIES OF GROUPS AROUND RX J1347.5−1145

Here we provide tables with properties of the optically selected group candidates around RX J1347.5−1145. Table B1 contains the optical properties of these groups, whereas in Table B2 we provide the derived X-ray properties for those groups with a detectable signal within the *XMM* field of view. Please see Sections 5.2 and 6 for additional details.
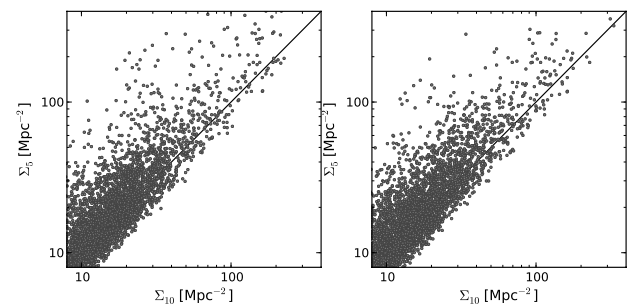
Figure A1. Comparison between Σ_{10} and the most commonly used Σ_5 (10 and five neighbours respectively) for two random Monte Carlo realization of the original catalogue. The line represents the one-to-one relation. Although both values correlate, a large scatter is evident.
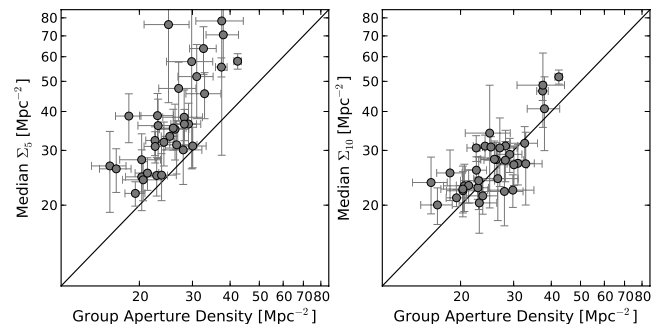
Figure A2. Comparison between the group mean density, measured within the aperture R_{group}, and the median Σ_5 and Σ_{10} for galaxies within the same aperture. The line represents the one-to-one relation. Error bars are the standard deviation from the 100 Monte Carlo realizations. It is clear that Σ_5 overestimates the density for almost all groups, either due to its sensitivity to small compact associations or projection effects in a photo-z-selected catalogue.

Table B1. List of the groups detected by the Voronoi tessellation technique. Columns: (1) identification number, (2) and (3) coordinates for the J2000 equinox, (4) radius of the overdensity, (5) and (6) average number of members and uncertainty, (7) and (8) fraction of blue galaxies and associated error, (9) and (10) total rest-frame *i*-band luminosity and error, (11) notes for individual clusters to provide a cross-identification.

(1) ID	(2) RA (J2000)	(3) Dec. (J2000)	(4) R_{group} (Mpc)	(5) $\langle N \rangle$	(6) $\sigma(N)$	(7) $\langle F_{blue} \rangle$	(8) $\sigma(F_{blue})$	(9) L (10^{11} L$_\odot$)	(10) Error (L) (10^{11} L$_\odot$)	(11) Notes
1	13:47:12.2	−12:14:09	0.369	13.28	1.77	0.71	0.15	4.45	1.03	
2	13:46:40.0	−12:12:14	0.493	15.6	1.83	0.94	0.06	3.69	0.72	
3	13:46:08.8	−12:10:04	0.649	24.45	2.36	0.81	0.13	4.44	0.70	
4	13:46:42.0	−12:08:49	0.493	15.77	2.31	0.92	0.08	1.52	0.38	
5	13:48:52.0	−12:04:19	0.406	12.98	2.22	0.56	0.16	4.08	1.06	LCDCS 0836
6	13:45:53.2	−12:02:38	0.340	10.17	1.55	0.85	0.15	1.03	0.11	
7	13:45:47.7	−12:01:37	0.356	15.19	1.87	0.65	0.13	4.25	0.79	
8	13:46:03.6	−12:00:57	0.587	17.29	2.26	0.77	0.16	3.81	3.77	
9	13:46:43.9	−11:57:36	0.612	34.26	3.35	0.77	0.12	4.66	4.27	
10	13:45:44.4	−11:57:54	0.581	17.77	2.12	0.90	0.09	3.49	0.49	
11	13:46:26.8	−11:54:28	0.987	114.7	5.06	0.56	0.05	20.6	1.02	LCDCS 0825
12	13:45:55.2	−11:55:04	0.273	8.84	1.58	0.61	0.19	2.27	0.62	
13	13:46:51.8	−11:53:13	0.894	48.71	3.69	0.80	0.09	8.86	0.75	
14	13:46:34.0	−11:50:45	0.643	29.67	2.51	0.77	0.11	6.45	0.56	
15	13:47:18.4	−11:52:19	0.446	16.42	1.82	0.31	0.08	6.14	1.93	BGV 2006–042
16	13:47:13.9	−11:51:32	0.321	9.15	1.38	0.66	0.17	3.96	1.14	
17	13:47:24.7	−11:50:16	0.551	23.08	1.98	0.56	0.09	6.51	0.37	
18	13:47:09.1	−11:47:52	0.512	23.27	2.28	0.72	0.11	7.55	0.48	
19	13:47:31.6	−11:45:21	1.201	192.1	5.53	0.33	0.02	45.8	1.69	RX J1347.5-1145
20	13:46:57.8	−11:46:08	0.435	17.93	1.93	0.66	0.12	4.24	0.24	
21	13:47:47.0	−11:42:21	0.309	9.88	1.31	0.30	0.11	3.08	0.42	
22	13:47:09.1	−11:41:24	0.400	13.6	1.91	0.81	0.17	1.59	0.34	
23	13:45:56.8	−11:40:12	0.466	15.8	2.25	0.85	0.14	1.41	0.26	
24	13:47:33.6	−11:39:57	0.676	30.59	2.75	0.60	0.09	5.48	0.61	
25	13:47:51.6	−11:38:49	0.773	42.41	2.88	0.69	0.07	10.0	1.06	
26	13:48:18.0	−11:38:42	0.773	42.47	3.46	0.79	0.10	7.44	0.79	
27	13:45:54.9	−11:35:56	0.377	10.29	1.33	0.63	0.15	4.11	0.35	
28	13:48:18.9	−11:34:30	0.529	22.78	2.33	0.81	0.13	3.15	0.39	
29	13:47:46.5	−11:32:52	0.464	16.08	1.91	0.42	0.11	4.15	0.68	
30	13:48:26.8	−11:29:02	0.280	7.35	1.28	0.41	0.15	4.54	0.95	
31	13:48:30.0	−11:27:25	0.302	9.41	0.96	0.24	0.08	3.09	0.12	
32	13:48:22.5	−11:24:39	0.925	67.87	4.25	0.69	0.07	14.3	0.79	NE Clump
33	13:46:48.9	−11:23:34	0.379	12.04	2.02	0.75	0.19	2.78	0.67	
34	13:46:30.9	−11:19:08	0.427	11.68	1.80	0.79	0.18	3.71	0.65	

Table B2. X-ray fluxes and derived parameters for optically detected groups in the area covered by *XMM–Newton* observations. Columns: (1) identification numbers (same as in Table B1), (2) and (3) coordinates, (4) measured X-ray flux and error, (5) X-ray luminosity, (6) total mass within the (7) R_{200} radius, (8) flux significance.

(1) ID	(2) RA (J2000)	(3) Dec. (J2000)	(4) F_X (0.5–2 keV) (10^{-15} erg s^{-1} cm^{-2})	(5) L_X (10^{42} erg s^{-1})	(6) M_{200} (10^{13} M$_\odot$)	(7) R_{200} (Mpc)	(8) $\sigma(F_X)$
13	13:46:51.8	−11:53:13	2.77 ± 1.66	2.83 ± 2.08	3.22 ± 1.12	0.57	1.67
15	13:47:18.4	−11:52:19	3.65 ± 1.57	3.71 ± 1.96	3.83 ± 0.98	0.60	2.32
16	13:47:13.9	−11:51:32	1.12 ± 0.79	1.21 ± 1.04	1.87 ± 0.75	0.47	1.42
17	13:47:24.7	−11:50:16	3.26 ± 1.26	3.32 ± 1.57	3.57 ± 0.82	0.59	2.59
18	13:47:09.1	−11:47:52	2.14 ± 0.94	2.20 ± 1.18	2.74 ± 0.71	0.54	2.29
22	13:47:09.1	−11:41:24	1.13 ± 0.73	1.22 ± 0.96	1.87 ± 0.70	0.47	1.55
25	13:47:51.6	−11:38:49	1.80 ± 1.34	1.87 ± 1.71	2.47 ± 1.05	0.52	1.34
26	13:48:18.0	−11:38:42	5.72 ± 1.77	5.77 ± 2.19	5.08 ± 0.95	0.66	3.24
29	13:47:46.5	−11:32:52	2.53 ± 1.51	2.59 ± 1.90	3.04 ± 1.06	0.56	1.68

This paper has been typeset from a TEX/LATEX file prepared by the author.